Automated Detection and Depth Determination of Melt Ponds on Sea Ice in ICESat-2 ATLAS Data—The Density-Dimension Algorithm for Bifurcating Sea-Ice Reflectors (DDA-Bifurcate-Seaice)

Ute Christina Herzfeld[®], Thomas M. Trantow[®], Huilin Han, Ellen Buckley, Sinéad Louise Farrell[®], and Matthew Lawson

Abstract—As climate warms and the transition from a perennial to a seasonal Arctic sea-ice cover is imminent, understanding melt ponding is central to understanding changes in the new Arctic. National Aeronautics and Space Administration (NASA)'s Ice, Cloud and land Elevation Satellite (ICESat-2) has the capacity to provide measurements and monitoring of the onset of melt in the Arctic and on melt progression. Yet ponds are currently not identified on the ICESat-2 standard sea-ice products, in which only a single surface is determined. The objective of this article is to introduce a mathematical algorithm that facilitates automated detection of melt ponds in the ICESat-2 Advanced Topographic Laser Altimeter System (ATLAS) data, retrieval of two surface heights, pond surface and bottom, and measurements of depth and width of melt ponds. With ATLAS, ICESat-2 carries the first spaceborne multibeam micropulse photon-counting laser altimeter system, operating at 532-nm frequency. ATLAS data are recorded as clouds of discrete photon points. The Density-Dimension Algorithm for bifurcating sea-ice reflectors (DDA-bifurcate-seaice) is an autoadaptive algorithm that solves the problem of pond detection near the 0.7-m nominal along-track spacing of ATLAS data, utilizing the radial basis function for calculation of a density field and a threshold function that automatically adapts to changes in the background, apparent surface reflectance, and some instrument effects. The DDA-bifurcate-seaice is applied to large ICESat-2 datasets from the 2019 and 2020 melt seasons in the multiyear Arctic sea-ice region. Results are evaluated by comparison with those from a manually forced algorithm.

Manuscript received 1 October 2022; revised 13 January 2023 and 17 March 2023; accepted 6 April 2023. Date of publication 18 April 2023; date of current version 22 May 2023. This work was supported by the U.S. National Aeronautics and Space Administration (NASA) Earth Sciences Division under awards 80NSSC20K0975, 80NSSC22K1155, 80NSSC18K1439, and NNX17AG75G (Principal Investigator Ute Herzfeld) and 80NSSC20K0966 and 80NSSC17K0006 (Principal Investigator Sinead Louise Farrell). (Corresponding author: Ute Christina Herzfeld.)

Ute Christina Herzfeld, Thomas M. Trantow, Huilin Han, and Matthew Lawson are with Geomathematics, Remote Sensing and Cryospheric Sciences Laboratory, Department of Electrical, Computer, and Energy Engineering, University of Colorado Boulder, Boulder, CO 80309 USA (e-mail: ute.herzfeld@colorado.edu).

Ellen Buckley is with the Center for Fluid Mechanics, Brown University, Providence, RI 02912 USA.

Sinéad Louise Farrell is with the Department of Geographical Sciences and the Department of Atmospheric and Oceanic Science, University of Maryland, College Park, MD 20742 USA.

Digital Object Identifier 10.1109/TGRS.2023.3268073

Index Terms—Arctic sea ice, computational algorithm, cryospheric sciences, Ice, Cloud and land Elevation Satellite (ICESat-2), melt pond, satellite altimetry.

I. INTRODUCTION

S THE Arctic sea ice has been reported to reach historic A lows repeatedly [40], [45], [46], [48], [49], [50], the sea-ice cover is transitioning from a perennial to a seasonal ice [20], [49] and melt ponding is a key process. Perovich et al. [36] alert to the complexity of melt ponds and their evolution on the thinning sea ice. Predictions based on models diverge [17], [18], [19], [33], [44], [48]. Since any predictions are only as good as the data they are based on, observations are essential in understanding changes in the Arctic cryosphere and constraining models. Previous studies have demonstrated the importance of melt ponds on summer sea ice evolution [16], [37], [38], [55], and various in situ studies have monitored their seasonal evolution [36], [39], [41], [54]. Although satellite-based studies of melt ponds exist [2], [7], [42], [43], [53], there is limited information on the depth of melt ponds at an Arctic-wide level.

NASA's Ice, Cloud and land Elevation Satellite (ICESat-2), launched September 15, 2018, has the capacity to provide measurements and monitoring of the onset of melt in the Arctic and on melt progression [2], [6], [52]. Yet, ponds are not identified in the standard sea-ice data product ATL07 [23], [25]. ATL07 reports only a single-surface height, and in some cases, this height is determined as somewhere between the height of the surface and that of the melt-pond bottom [6]. The single-surface tracking of this product does not provide useful information on summer sea-ice melt ponds [23]. A segment-type parameter on ATL07 which can assume a value indicative of a surface class labeled as "lead/melt pond" is a potential source of error. Missing ponds or confusing ponds with sea-ice leads can result in miscalculation of freeboard, which is reported in ICESat-2 data product ATL10 [24], see [6].

What appears to be a discrepancy between the observation capabilities of the sensor and the current status of official data

1558-0644 © 2023 IEEE. Personal use is permitted, but republication/redistribution requires IEEE permission. See https://www.ieee.org/publications/rights/index.html for more information.

products can be explained by a combination of the spatial scale of change signals in Arctic sea ice and mathematical algorithms applied in data analysis. With the Advanced Topographic Laser Altimeter System (ATLAS), ICESat-2 carries the first spaceborne multibeam micropulse photon-counting laser altimeter system. ATLAS registers returns from every photon in the 532-nm (green light) spectral band of the sensor, including photons from ambient light (background photons) in addition to signal photons, which together form a photon point cloud, reported on the product ATL03 [30], [31], [32]. The nominal along-track photon spacing is 0.7 m (under clear-sky atmospheric conditions), calculated from the ≈7-km/s along track the velocity of the satellite and the ATLAS sensors' pulse-repetition frequency of 10 000 pulses per second [13], [32].

The sea-ice ICESat-2 ATLAS data products ATL07 and ATL10 [24], [25] have facilitated significant findings on sea-ice freeboard and seasonal changes for the entire Arctic and Antarctic sea-ice regions [21], [22]. The mathematical algorithms applied to derive the ICESat-2 ATLAS sea-ice products [22], [23], which are based on a deconvolution assuming a Gaussian surface height distribution, yield information per along-track segment area, whose length depends on fixed 150 photon counts, and thus, is variable, typically between 17 m \times 27 m and 17 m \times 200 m [22], which then significantly reduces the spatial resolution of surface heights and freeboards reported on the sea-ice products compared with the original ATL03 data. The resultant products ATL07 and ATL10 have a spatial resolution that is sufficient for documentation and analysis of changes in the entire Arctic or Antarctic regions [21], [22], but not for detection of melt

Analyses of ATL03 data collected over Arctic sea ice show that melt ponds, snow depth, ridged, and rubbled ice are resolved in the photon cloud, which suggests that geophysical processes can be studied that lead to the formation of these high-resolution signatures in the ice [2], [6], [52]. To automatically detect and report melt ponds in ICESat-2 ATLAS data and measure their depth, a new algorithm needs to be developed that builds on the ATL03 photon cloud. In this article, we introduce such an algorithm.

More formally, a high-resolution algorithm that facilitates retrieval of two surfaces wherever such are recorded is required to report melt-pond existence and depth from ICESat-2 data. In order to allow operational application for ICESat-2 photon data across large and small regions alike (including the entire Arctic and Antarctic sea-ice regions), such a melt-pond algorithm (MPA) needs to be designed to meet the following criteria.

- 1) The algorithm needs to be fully automated (i.e., it should not require a priori information on the existence or location of a pond).
- 2) Detect ponds wherever returns from both pond bottom and pond surface are recorded in ICESat-2 photon data.
- 3) Avoid false positives.
- Automatically adapt to different background characteristics of daytime and nighttime data and to changes in apparent surface reflectance (ASR).

- 5) Find ponds among sea ice of different roughness types (smooth, ridged, and complex).
- 6) Correctly determine the start and end points of a pond along the ICESat-2 ground track.
- 7) Measure the pond depth.
- 8) Represent the complexity of the sea ice at high resolution.

In this article, we introduce an algorithm for melt-pond detection from ICESat-2 data that satisfies the above-mentioned criteria, building on our concept of the Density-Dimension Algorithm (DDA) for ICESat-2 data analysis [9], [11], [12], [13], which facilitates ice-surface height determination at the 0.7-m nominal resolution of the sensor (under clear-sky atmospheric conditions). The new sea-ice algorithm is termed DDA for bifurcating sea-ice reflectors (DDA-bifurcate-seaice or DDA-bif-seaice for short).

The complexity of the task of automated melt-pond detection and depth measurement is illustrated in [36, Figs. 3 and 11], who collected mass-balance measurements during the Surface Heat Budget of the Arctic Ocean (SHEBA) experiment conducted October 1997–October 1998. A simple algorithm for depth measurement of ponds has been described and applied in [3], [6] and [4] [UMD-melt-pond-algorithm (MPA)]. Their algorithm requires knowledge where a pond exists, it is not automated and thus cannot be employed for operational processing of ICESat-2 products.

This article will include a mathematical description of the DDA-bif-seaice and its application to ICESat-2 data from the Lincoln Sea. The DDA-bif-seaice will be applied to analyze ICESat-2 ATLAS data from melt-pond regions in the Lincoln Sea and other parts of the multiyear ice regions of the Arctic Ocean.

As a means of evaluation, results from the DDA-bif-seaice will be compared with results from a simple algorithm for analysis of melt ponds in ICESat-2 ATLAS that requires a-priori manual identification of ponds, developed at the University of Maryland (UMD MPA). The UMD MPA, described in [1] and [5], is not automated, and thus, cannot be employed for the operational processing of ICESat-2 products.

The DDA-bif-seaice is applied in a large-scale analysis of ICESat-2 ATLAS datasets to study melt onset and the evolution of melt ponds on multiyear sea ice in the Arctic, reported in a companion paper [5] that also uses the UMD MPA.

II. ICESAT-2 IN A NUTSHELL

A. Main Characteristics of Instrumentation, Observation, and Resultant Data

ICESat-2 ATLAS is a micropulse photon-counting laser altimeter system, which collects data in three pairs of two beams, a strong beam and a weak beam, where the energy of the weak beam is a quarter of that of the strong beam [27], [32]. Across-track separation of the beams on the Earth's surface is 3.3 km between the centers of adjacent pairs and 90 m for the beams within each pair. The ICESat-2 observatory yields observations through a complex geometry, illustrated in [13, Fig. 3 and Table 1], the strong beam in a pair of

beams can be either the right beam or the left beam (e.g., gt2r or gt2l), depending on whether ATLAS flies forward or backward (orientation changes every few months). The sensor operates in the 532-nm wavelength (green light) with a pulse-repetition rate (PRF) of 10 kHz. The PRF combined with the satellite's along-track velocity of \approx 7 km/s results in a nominal 0.7-m spacing of the laser pulses on the Earth's surface, under clear-sky atmospheric conditions. ATLAS has a footprint diameter of less than 17.4 m at 85% encircled energy. The field of view (FOV) of the receiver telescope is 83.8 μ rad, equivalent to 45-m FOV on the surface of the Earth. Observatory performance has been assessed in [26], where the actual footprint is characterized as closer to 11 m in diameter. As the FOV moves along the satellite ground track and returns from every single photon (in the 532-nm wavelength domain of the sensor) are recorded, surface structures at a much higher resolution than footprint diameter can be resolved (see Sections III and V and [13]). We, therefore, refer to the resolution of the ATLAS data as the nominal 0.7-m alongtrack spacing (under clear-sky atmospheric conditions), for the brevity of terminology, keeping in mind details on the derivation of the photon point cloud.

The instrumentation and derivation of the recorded photon point cloud are described in [32], and any technical component of the instrument and dataset necessary for understanding the work in this article is found in [13]. Information in this section is modified after [14], where the validation of the ICESat-2 data collection over complex land ice surfaces is performed.

In addition to the photons that result from the active lidar signal (signal photons), the photon point cloud also includes background photons that stem from ambient light in the 532-nm range of the spectrum and artifacts due to instrument effects, such as dead-time effect and afterpulses. The identification of signal photons in the point cloud or classification of signal versus background photons constitutes an ill-posed mathematical problem.

B. Standard ICESat-2 ATLAS Sea-Ice Products: ATL07 and ATL10

The current standard data products for sea ice are ICESat-2 ATLAS products ATL07 Sea Ice Height [25] and ICESat-2 ATLAS ATL10 Sea Ice Freeboard [24]. The derivation of the standard sea-ice data products ATL07 and ATL10 is described in the algorithm theoretical basis document (ATBD) for ATL07 and ATL10 [23] and in [22]. The ATL07 algorithm is not based on a fixed spatial resolution, but rather on a fixed number of recorded photons, which results in sea-ice height determinations of variable size. The ATL07 algorithm is aimed at resolving a single-surface height. Thus, it does not resolve melt ponds. The determination of sea-ice freeboard can also be affected by errors in the surface height determination [6].

III. OVERVIEW OF THE APPROACH DDA-BIF-SEAICE AND EXAMPLES OF MELT-POND DETECTION

The central objective of this article is to introduce the DDA-bifurcate-seaice and apply it to the detection and depth determination of melt ponds in Arctic sea ice. A first view

of the results of the DDA-bif-seaice is given in Fig. 1, which illustrates that ponds can be detected across a range of different environments indicated by different surface morphologies, as well as for the central and outer beams of the ATLAS instrument. The fact that ponds are found in situations of highly variable ASR, indicated by the colors of the signal photons in Fig. 1, points at the autoadaptive capability of the algorithm, which allows detecting bifurcating and rejoining surfaces in presence of different ASR levels.

Fig. 1(a) shows a large (over 200-m diameter) melt pond that is located among ridged sea ice and has a complex bottom topography, Fig. 1(b) illustrates the detection of shallow and relatively deep (3 m) ponds among smooth and ridged ice. The right pond (at 335 800) is located among fault blocks, in a location that is typical for the formation of melt ponds, and thus, is of interest for process studies. From the view point of a detection algorithm, the sequence of ponds in Fig. 1(b) illustrates a set of bifurcation points (points where one sea-ice surface splits into two surfaces of the melt-pond top and the melt-pond bottom) and rejoining points (where the two surfaces come together at the end of a melt pond). The set of bifurcation and rejoining points will be identified in the DDA-bif-seaice algorithm to facilitate the identification of individual points, tracking of ponds across analysis steps, and calculation of statistical values, such as depth (range) and pond width (in the alongtrack direction). Ponds are identified in situations of weak surface reflectance [e.g., Fig. 1(e), (g), and (h)], strong surface reflectance [Fig. 1(b), (c), and (f)] with density values of 250, and mixed-surface reflectance [Fig. 1(a)]. Ponds can be identified in the outer beams, for example, in gt31 in Fig. 1(a) and (d)-(f) and in gt11 in Fig. 1(b) and (c), as well as in the center beam, gt2l, in Fig. 1(g) and (h). All examples in Fig. 1 stem from strong beams, but ponds are also detected in data from the weak beam.

The examples may also serve to provide a first understanding of the tasks that the DDA-bif-seaice performs and as such motivate the mathematical description of the algorithm, given in Section IV.

Following the mathematical description, the DDA-bif-seaice will be applied to data from the multiyear Arctic sea-ice region, for two different years, 2019 and 2020, during the melt season (Section V). Corrections for the speed of light in sea water to calculate the depth from range and challenges for the algorithm are discussed in Section V as well. Results from the DDA-bif-seaice will be compared with results reported on the ICESat-2 standard product ATL07 to demonstrate the increase in information content.

IV. ALGORITHM: DDA-BIFURCATE-SEAICE

A. Family of Density-Dimension Algorithms

The DDA-bifurcate-seaice is part of the DDA family. The DDAs have been developed for the analysis of micro-pulse photon-counting lidar altimeter data, especially data collected with the ICESat-2 ATLAS instrument and its airborne predecessors such as the Sigma Space lidar, the Multiple Altimeter Beam Experimental Lidar (MABEL)

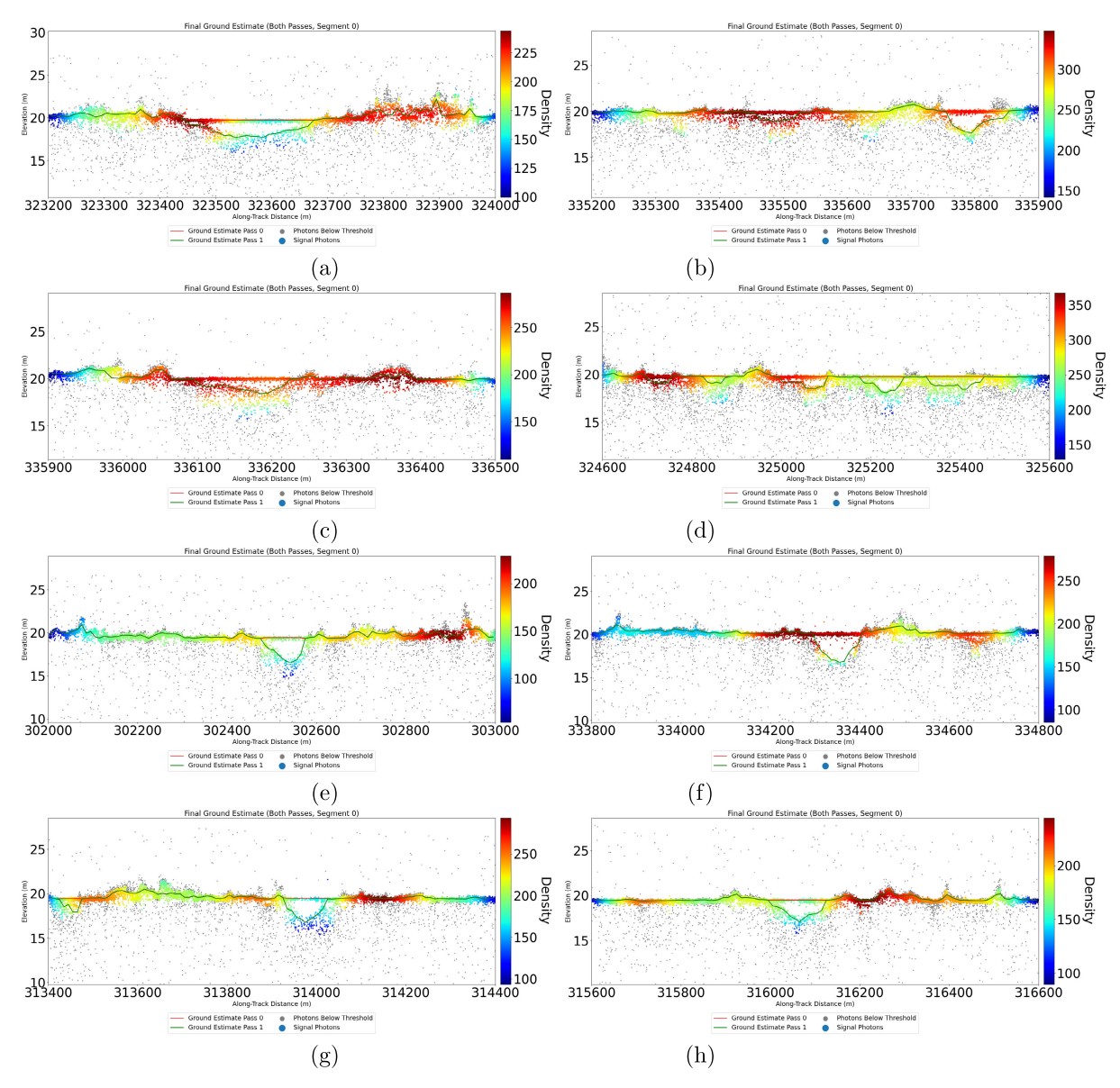


Fig. 1. Examples of ponds detected with the DDA-bif-seaice in summer 2019 ICESat-2 ATLAS data, Multi-year Arctic sea-ice region. Lincoln Sea. All ponds from strong beam data. (a) Pond among ridges with variable density at top. Surface follower (top) not optimized for ridges [1237 gt31 82.818.png (mega 3)]. (b) Several ponds detected-shows bifurcation and rejoining points (1237 gt11 82.906.png). (c) Not a false positive-bottom of pond has variable topography (1237 gt11 82.906 2.png). (d) Complex regions with several ponds. Note rightmost pond is barely a pond in the making [1237 gt31 82.831.png (mega 4)]. (e) Perfect pond [1298 gt31 82.637.png (mega 1)]. (f) Perfect pond below strongly reflecting surface (density 250) [1298 gt31 82.911.png (mega 2)]. (g) Pond among complex sea-ice topography. Center beam (gt2l) (1298 gt2l 82.745.png). Examples in 1a, b, c, d, e are from ICESat-2 ATLAS granule ATL03 20190618062235 12370304 005 01.h5, reference ground track (RGT) 1237, collected 2019-June-18, ICESat-2 ASAS version 5 data set. Examples in 1f, g, h are from ICESat-2 ATLAS granule ATL03 20190622061415 12980304 005 01.h5, RGT 1298, collected 2019-June-22, ICESat-2 ASAS version 5 data set.

and the Slope Imaging Multi-polarization Photon-counting Lidar (SIMPL), and include algorithms for ice surface data (the DDA-ice) [12], [13], [14], for vegetation data (the DDA-sigma-veg) [10], and for atmospheric layers (the DDA-atmos) [9], [11]. Common to all DDAs is the ability to retrieve surfaces and other reflectors in situations of complex spatial data distributions and mathematically difficult signal-to-noise relationships. Examples include crevassed and otherwise morphologically complex ice surfaces, vegetation canopy and ground under canopy, and tenuous atmospheric layers such as optically thin clouds, blowing snow and aerosol layers. The DDA-atmos is the algorithm applied for the identification of

atmospheric layers and surface in the ICESat-2 atmospheric data product, ATL09 (see also [34]).

B. DDA-Ice Mathematical Philosophy

The DDA-bif-seaice builds on the DDA for ice surfaces (DDA-ice or DDA-ice-1). The DDA-ice is the original algorithm for ice surfaces and the name DDA-ice-1 indicates that it follows a single surface (more technically, the DDA-ice-1 performs a single-density run).

The main idea of the DDA-ice is that signal photons are expected to have a neighborhood with a larger photon density than background photons. To quantify density, photons are aggregated using a Gaussian *rbf*. A *rbf* is a real-valued function whose value decreases with distance from the center *c*

$$\Phi(x,c) = \Phi(\|x-c\|) \tag{1}$$

for all $x = (x_1, x_2)$ with along-track location and height coordinates (x_1, x_2) in a definition area \mathcal{D} with respect to any norm $\|\cdot\|$. The density field of the photon cloud is calculated by letting every single photon take the role of a center $c = (c_1, c_2)$ with coordinates (c_1, c_2) , evaluating the *rbf* for all neighboring photons and forming the sum of weights from this process [12]. This concept is especially useful for data aggregation in the photon analysis problem because points closer to the center are given a larger weight than points farther away.

Density is considered a dimension of the dataset, in addition to location. Signal-background separation is performed by an autoadaptive threshold function in the geolocation-density domain. The threshold function is formulated using discrete mathematics: Starting from the set of all photon points in a height slab that contains the signal of largest counts at large scale, the threshold function sorts candidate photons for signals into different sets, using mathematical and statistical criteria based on density and geolocation. The autoadaptive capability of the algorithm implies that a threshold function is used which automatically adapts to the variable background characteristics of day-time and night-time observations in the photon point cloud (a lot more photons from ambient light are recorded during day-time), ASR, and other, including instrumental, sources of background photons. The results of the DDA-ice-1 are not disturbed by instrument-related background photons, such as those resultant from after-pulses (because these are less dense than the surface signal). Surface height among and between signal photons is determined using a ground follower, a function that automatically adapts to surface roughness. The option for areas of high surface roughness, originally designed for surface-height determination over crevassed glaciers, facilitates surface-height determination of ridged and rubbled seaice, while the option for low surface roughness works well for simple, smooth surfaces of marine and terrestrial ice environments [12], [13]. The DDA-ice-1 resolves surface heights at the resolution of the sensor, i.e., of the point-cloud data (nominally 0.7-m along-track) and height segments of 5 or 2.5 m, depending on surface roughness [13]. While an individual photon point represents a measurement from an approximately 11-m-diameter footprint, the analysis is based on the photon point cloud, and the information in the point cloud allows us to retrieve much more spatial detail of a surface than points spaced 11 m would. The DDA utilizes a data aggregation technique, which helps reveal the high-resolution spatial variability in the point cloud. Herein lies the power of the DDA as a data aggregation method as opposed to classical statistics. The ground follower naturally reduces the resolution of the output somewhat.

C. Input Data, Algorithm Development, and Version

As input for analysis, the DDA-bifurcate-seaice uses the geolocated photon point cloud, which includes signal and background photons, as reported in the ICESat-2 ATLAS

ATL03 data product [30], [31], [32]. The DDA algorithms do not use the photon classification that is provided on ATL03 [13]. Simply speaking, the photon classification on ATL03 often fails to properly identify signal photons in situations of crevassed or otherwise morphologically complex cryospheric terrain for the strong beam and the weak beam, and the DDA-ice does not require classified photons as input, but carries out a signal-noise separation as part of the algorithm [13]. The ATL03 datasets are publicly available via the NASA Earthdata site and updated at regular time intervals of about six months.

Analyses in this article utilize the ICESat-2 ATLAS data products ATL03 (ATLAS/ICESat-2 L2A Global Geolocated Photon Data), version 5 [30], described in the ATBD for ATL03 [31].

The algorithm DDA-bif-seaice was developed on local desktops (iMacs) of the Geomathematics, Remote Sensing and Cryospheric Sciences Laboratory, University of Colorado at Boulder, Boulder, CO, USA, the computational code is implemented using python 3. The algorithm described in this article is that of DDA-ice geomath version v18.0 (latest version as of June 2022; committed December 2021).

For the processing of large amounts of ICESat-2 ATLAS collected over the multiyear Arctic sea-ice region, the DDA-ice-bifurcate was transferred to the NASA cloud (ADAPT). Results are reported in the companion paper on the evolution of melt ponding [5]. An advanced version of the DDA-bif-seaice algorithm may be included in a future version of the standard ICESat-2 products.

D. Challenges Specific to Melt-Pond Detection Over Seaice

The occurrence of melt ponds is by no means specific to sea ice, as melt ponding occurs over glaciers, ice sheets, and snow fields as well [8]. There are, however, challenges specific to melt-pond detection over sea ice, which warrant the development of a specific sea-ice algorithm. We have developed an algorithm for bifurcating reflectors, aimed at the detection of large melt ponds on the Amery Ice Shelf and for the detection of melt ponds and channels on the Greenland Ice sheet. The ponds on land ice and ice shelves are much larger (kilometers to tens of kilometers) and deeper than those on sea ice; thus, the identification of bifurcation and rejoining locations of the two surfaces, pond surface, and pond bottom, is naturally much more robust to the selection of algorithm-specific parameters that determine the resolution, and false positives are avoided relatively easily. The situation for sea ice is much more complex. Ponds can form in smooth sea-ice regions as well as in ridged ice areas, where ponds typically occur on the side of a faulted sea-ice block. The ridge height is often larger than the pond depth, creating an additional challenge for an automated detection algorithm.

An additional challenge is due to the fact that sea ice is, simplified, stratified into frozen seawater overlain by a snow layer, and the two layers interact differently with the incoming lidar signal. The penetration, scattering, and reflection properties of lidar signals in complex media are far from understood (see [47]). As melting progresses, snow and ice transform into slush, forming sea-ice ponds in the making,

Authorized licensed use limited to: UNIVERSITY OF COLORADO. Downloaded on June 09,2023 at 22:19:57 UTC from IEEE Xplore. Restrictions apply.

which can already be seen in the lidar signal [for example, in Fig. 1(d)]. Other examples illustrating the complexity of sea ice include ponds with a solidly frozen surface, where a pond formed and the surface refroze, subnivean ponds, ponds with solid bottoms [Fig. 1(a)] and ponds with ill-defined bottoms [Fig. 1(c)]. For imagery of sea ice as well as other remotesensing observations, we refer to [15] and [29], [51].

We have previously developed a second-order algorithm, the DDA-ice-2, for the case that the stronger reflecting surface is always on top. For the melt-pond detection problem, this assumption cannot be made. The stronger reflecting surface can be the top of a melt pond or its bottom, or both surfaces can be of similar strength, or the strength of the reflector may even switch from top to bottom depending on location. These complexities of the problem motivate the development of a DDA-bifurcate for the analysis of lidar data over sea ice.

A key challenge in designing a melt-pond-detection algorithm for photon-cloud data (such as ATL03 data) lies in the identification of bifurcation locations of the reflecting surfaces and in the identification of locations where the two surfaces rejoin (rejoining locations). The bifurcation algorithm needs to be robust w.r.t. the distribution of the point-cloud data: 1) to identify small and shallow ponds, with the goal of vertical resolution of 0.1 m and 2) to avoid false positives (locations that show point clusters at two or more different heights, where a pond does not exist).

A problem that is especially severe in the analysis of sea-ice data is posed by the occurrence of signal saturation, which in combination with the detector dead-time effect leads to delayed registration of photons, resulting in apparent secondary layers below the actual surface at (pseudo) depths that overlap with typical depths of melt ponds on sea ice. There are several such pseudodepths, at 0.43 m and farther below. This problem is addressed in Section V-C.

E. Algorithm Steps of the DDA-Ice-1

The DDA-bif-seaice builds on the DDA-ice-1 (there called the DDA-ice), the algorithm for primary surface detection, as described in [12]. Here, we describe the algorithm to the extent necessary to understand the concept of the DDA-bif-seaice. The algorithm steps are illustrated in Fig. 2 for an example of ATLAS data over sea ice. The algorithm is driven by a set of algorithm-specific parameters, described in [12]. Parameters, specific to the DDA-bif-seaice and the analysis described in this article, are given in Table I.

The DDA-ice-1 has the following steps.

- 1) Large-scale separation of signal and noise slabs.
- 2) Calculation of the density field using the radial basis function, *rbf*.
- Operation of an autoadaptive threshold function to separate noise and signal photons, using density as an additional dimension.
- 4) Application of a piecewise linear ground follower with 1–10-m resolution over smooth surfaces and 0.5–5 m over crevasses, sastrugi, and other rough surfaces. The ground follower automatically adapts to surface roughness.

(Step 1) Separation of Signal and Noise Slabs: The large-scale separation of signal and noise slabs utilizes a simple histogram-based criterion that evaluates photon counts. The signal slab centers in height around the height bin of strongest return (highest photon count) and the noise slab is determined as the slab of the same height interval located immediately above the signal slab. For sea ice, bin sizes are 50 m along-track and 10 m in height, and the slab thickness is 30 m for the resultant signal and noise slabs (see Table I).

(Step 2) Calculation of the Density Field: The density field is calculated for every single photon, using that photon as the center point, c of a kernel. The description follows [12]. A Gaussian rbf, formally defined in (1), is evaluated as follows, letting r = x - c and $s \in \mathcal{R}$:

$$\Phi(r) = \frac{1}{\sqrt{2\pi s^2}} e^{-\left(\frac{r}{\sqrt{2}s}\right)^2}.$$
 (2)

The *rbf* has the shape of (half) a Gaussian bell curve rotated around the location of a center $c \in \mathbb{R}^2$.

Using

$$f_{\text{normpdf}} = \frac{1}{\sqrt{2\pi\sigma^2}} e^{-\left(\frac{x-\mu}{\sqrt{2}\sigma}\right)^2} \tag{3}$$

with standard deviation σ and mean μ of a statistical population and replacing $\sigma = s$ and $\mu = 0$ yields (4)

$$\Phi(r) = f_{\text{normpdf}}.$$
 (4)

For each point in the definition set \mathcal{D} (each photon in the cloud, for both signal and noise slabs), a density value $f_d(c)$ is calculated as

$$f_d(c) = \sum_{x \in \mathcal{D}_c} W_c(x) \tag{5}$$

for all x within the search region \mathcal{D}_c , where the weights $W_c(\cdot)$ are derived from the rbf as

$$W(c, x) = W_c(x) = \Phi(\|x - c\|)$$
 (6)

with $x \in \mathcal{D}_c$ (see [12, eq. (11)]).

Algorithm-Specific Parameters: The kernel of the rbf is controlled by the algorithm-specific parameters standard deviation σ , anisotropy a, and cutoff κ , where κ is the number of standard deviations used to define the extent of the search region. For $a \neq 1$, points with the same rbf value $\Phi(\|x - c\|_a)$ are located on an ellipsoid with axes (a, a, 1) around the center point c, rather than on a circle. In the original DDA, anisotropy is selected such that the resultant ellipsoid has a longer axis parallel to the horizontal, motivated by the idea that the probability of finding more ground signal points is larger in the approximately horizontal direction than in the vertical direction; for the validation of this concept and examples from the ICESat-2 airborne simulator, SIMPL data, see [12]. The fact that typical sea ice has a large horizontal extension motivates the use of a large anisotropy factor of a = 20.

With anisotropy, the density value, $f_{d,a}(c)$, is calculated as

$$f_{d,a}(c) = \sum_{x \in \mathcal{D}_{c,a}} W_{c,a}(x). \tag{7}$$

TABLE I

ALGORITHM-SPECIFIC PARAMETERS FOR THE DDA-BIFURCATE-SEAICE. THIS TABLE LISTS ALL PARAMETERS AND THEIR VALUES USED TO RUN DDA-BIF-SEAICE, INCLUDING THOSE OF THE DDA-ICE-1. CODE VERSION V.122 (JUNE 2022). STRONG BEAM AND WEAK BEAM—ATLAS BEAMS. SYMBOL (-) GIVEN FOR COMPUTED PARAMETERS. PARAMETER VALUES AS USED FOR ALL EXAMPLES GIVEN IN THIS ARTICLE AND FOR THE MELT-POND EVOLUTION STUDY, 2020. THE DATA ANALYSIS UTILIZES THE SAME PARAMETERS FOR THE STRONG BEAM AND THE WEAK BEAM, BUT DIFFERENT PARAMETERS CAN BE USED. THE OPTION "USING DENSITY HISTOGRAMS?"

REFERS TO AN ALTERNATIVE ALGORITHM THAT IS NOT USED IN THIS ANALYSIS

symbol	meaning	strong beam	weak beam
math		ATLAS	ATLAS
(code)		(actual)	(actual)
	parameters for DDA-ice-1		
numpass	number of passes	1	1
σ (s)	standard deviation	3	3
κ (u)	cutoff	2	2
a (a)	anisotropy	20	20
-	kernel width in meters (pass0)	240.0	240.0
-	kernel height in meters (pass0)	12.0	12.0
1	slab thickness (m) for signal and noise slabs	30	30
pix (vector)	pixel-size for histogram-based slabs (m)	[50, 10]	[50, 10]
$t_{bin}(\mathbf{b})$	bin-width for thresholding	5	5
$t_{\it offset}({ m k})$	threshold offset	1	1.0
q	threshold quantile	0.15	0.15
R	resolution of ground follower (m)	10	10
r	factor to reduce the R parameter	2	2
-	resolution of ground follower for rough surfaces (m)	5	5
Q	crevasse depth quantile	0.5	0.5
S	standard deviation threshold	1.75	1.75
	of thresholded signal to trigger		
	small step size in ground follower (m)		
	data handling information		
С	data chunk size (in along-track meters)	3000	3000
	photon data read as	[dt, lon, lat, elev]	[dt, lon, lat, elev]
	additional parameters for DDA-bif-seaice		
m	DDA-bifurcate (melt pond) run?	1=true	1=true
mp_bin_h (z)	horizontal bin size (DDA-bif) (m)	25.0	25.0
mp_bin_v (v)	vertical bin size (DDA-bif) (m)	0.1	0.1
dq	meltpond quantile (DDA-bif)	0.75	0.75
D	using density histograms? (DDA-bif)	0=false	0=false
M	minimum peak in histograms (DDA-bif)	3.0	3.0
О	minimum prominence in histograms (DDA-bif)	3.0	3.0

This calculation is carried out for each photon as a center point and yields the density field.

(Step 3) Threshold Function: An autoadaptive threshold function, described in [12], is employed to separate signal and noise photons. The threshold function is controlled by a quantile and threshold offset as algorithm-specific parameters (see Table I).

In this algorithm version (DDA-ice-py3, v18.0) we use a two-step threshold function. In the first step, the maximum density values of photons in the noise slab are calculated, and photons with a density value larger than this maximum plus a threshold-offset value are passed into a set. In the second step, the q-quantile of this set is passed into a second set. The second set forms the set of ice-surface signal photons.

Mathematically, this reads as follows (summarized from [12]).

Threshold-determination is carried out in along-track bins of size $t_{\rm bin}$, with $t_{\rm bin}=5$ m for the melt-pond analysis in this article. For each bin, indexed by s, the maximal value of density for all points in the noise slab $\mathcal{D}_{{\rm noise},s}$ for this bin is found according to

$$f_{\text{max,noise},s} = \max \{ f_{d,a}(c) \mid c \in \mathcal{D}_{\text{noise},s} \}$$
 (8)

using (7) for the density value $f_{d,a}(c)$. Next a first threshold-value $t_{s,1}$ is calculated as

$$t_{s,1} = f_{\text{max,noise},s} + t_{\text{offset}} \tag{9}$$

by adding a global threshold offset $t_{\text{offset}} \in \mathcal{R}$ to the maximal density value found in the noise slab.

We define the set T_s as the set of all photon returns (center points) c in the corresponding bin in the signal slab $\mathcal{D}_{\text{signal},s}$ with density value larger than the first threshold $t_{s,1}$

$$\mathcal{T}_s = \{ f_{d,a}(c) \mid c \in \mathcal{D}_{\text{signal},s} \land f_{d,a}(c) > t_{s,1} \}. \tag{10}$$

A second threshold $t_{s,2}$ is defined as the q-quantile of the set \mathcal{T}_s , i.e., $t_{s,2} = v$ for the value v for which the density value satisfies

$$f_{d,a}(c) < v \tag{11}$$

for a fraction $0 \le q \le 1$ of the points c in the set T_s .

Then, a photon in bin s of the signal slab is identified as an ice-surface return if the density value of the photon is larger than the q-quantile of the set \mathcal{T}_s , i.e., if

$$f_{d,a}(c) > t_{s,2} \tag{12}$$

defining the set of ice-surface returns in along-track bin s as

$$S_s = \{c \mid c \in T_s \land f_{d,a}(c) > t_{s,2}\}. \tag{13}$$

The autoadaptive thresholding process is illustrated in Fig. 2. The analysis uses $t_{\rm offset} = 1$ and q = 0.15.

The set of all ice-surface returns is the joint set of S_s for all along-track bins

$$S = \{c \mid c \in S_s, s \in \mathcal{J}\}$$
 (14)

for the index set \mathcal{J} of all threshold-bin indices.

After the application of the threshold function, surface height is given by the height values of individual photons that are classified as signal photons. The output of the threshold function has the same resolution as the originally registered photons (without background photons), reported on ATL03, and therefore, the spatial resolution of the output of the DDA-ice at this step is the same as the nominal 0.7-m resolution of ATLAS. This is possible because the DDA-ice utilizes a data aggregation, not a data averaging operation.

(Step 4) Roughness-Controlled Piecewise linear Ground Follower: For users interested in surface height at a given location or users who prefer a continuous line of surface heights over heights at individual photon locations, a piecewise linear ground follower is applied. The terminology "roughnesscontrolled piecewise linear ground follower" is a simplified description of a mathematical interpolator that builds on the segmentation of an interval into short sections where the surface is rough and into larger sections where the surface is smooth. The height determination rules are summarized as follows: if the standard deviation of the photons determined as signal photons (in Step 3) in a given along-track segment of length R (here: R = 10 m) exceeds a value S (the standard deviation for the ground follower), then the smaller stepsize, calculated as $\frac{R}{f}$ is used for the piecewise linear interpolator. The height determination employs a density-weighted interpolator [12, eq. (30)], which allows placing the surface height depending on surface properties.

Determination of Algorithm-Specific Parameters (Sensitivity Studies): The values of the algorithm-specific parameters are determined in a sensitivity study. A sensitivity study is a stepwise optimization process, during which parameters are varied one at a time, holding the rest of the parameter set constant around a control parameter set (typically the last

parameter set used in successful data analysis). Once a new optimal solution is found, this is set as the control set, and the next iteration, varying each parameter, is carried out. Iterations are continued until a satisfactory parameter set has been determined, aided by experience in photon-counting lidar data analysis or validation data.

Data Handling Information: Version v18.0 of the DDA-ice-py3 allows processing of large files (entire ICESat-2 ATLAS granules). This is facilitated by so-called "chunking," an operation that loads segments of the datasets (here: 3000 m along-track). Chunking requires involved handling of data and intermediate algorithm results when passed to subroutines, to avoid effects at "chunk" boundaries. The mathematical details of the chunking algorithm developed specifically for the DDA-bif-seaice algorithm go beyond the objectives of this article.

Photon data are read in as

(dt, lon, lat, elev).

Photon data are appended with distance along track as (delta time, lon, lat, elev, distance).

F. Algorithm Steps of the DDA-Bifurcate-Seaice (DDA-Bif-Seaice)

The idea of a bifurcating algorithm is to identify locations where two geophysically valid surfaces exist, here, the top and bottom of a melt pond on sea ice. Two surfaces can clearly be identified in ICESat-2 data in some situations, but less clearly in others. Implementation of this simple concept as an automated algorithm has several complications, due to the complexity of: 1) the melt ponding process and 2) the lidar observations (interactions of the lidar signal with complex cryospheric materials, including snow, ice, slush, and water). As discussed in Section IV-D, the cryospheric materials undergo a metamorphosis during the melt process, and the different materials resulting from the stages of this metamorphosis result in different returns of the lidar signal, manifested in the spatial distribution of photons in the point cloud. The ATL03 data can show many stages of "ponds in the making." The question is then, at which stage should an algorithm identify two surfaces and call out a pond? Determination of the location of a bifurcation and rejoining point is a third problem.

Critical to these problems as part of an algorithm is the determination of spatial resolution. The current analysis uses a horizontal resolution of 25 m and a vertical bin size of 0.1 m in the bifurcation criterion, which strikes a balance between the conflicting goals of finding enough signal photons to identify bifurcations while avoiding false positives. Pond bottom depths (and ice-surface heights) are resolved at 5-m and 10-m along-track resolution for rough and smooth surfaces, respectively, with the smallest detectable ponds of 15- and 30-m widths. The values have been determined in sensitivity studies.

In the following, we describe how the bifurcation algorithm for sea-ice data is interleaved into the DDA-ice-1. Algorithm

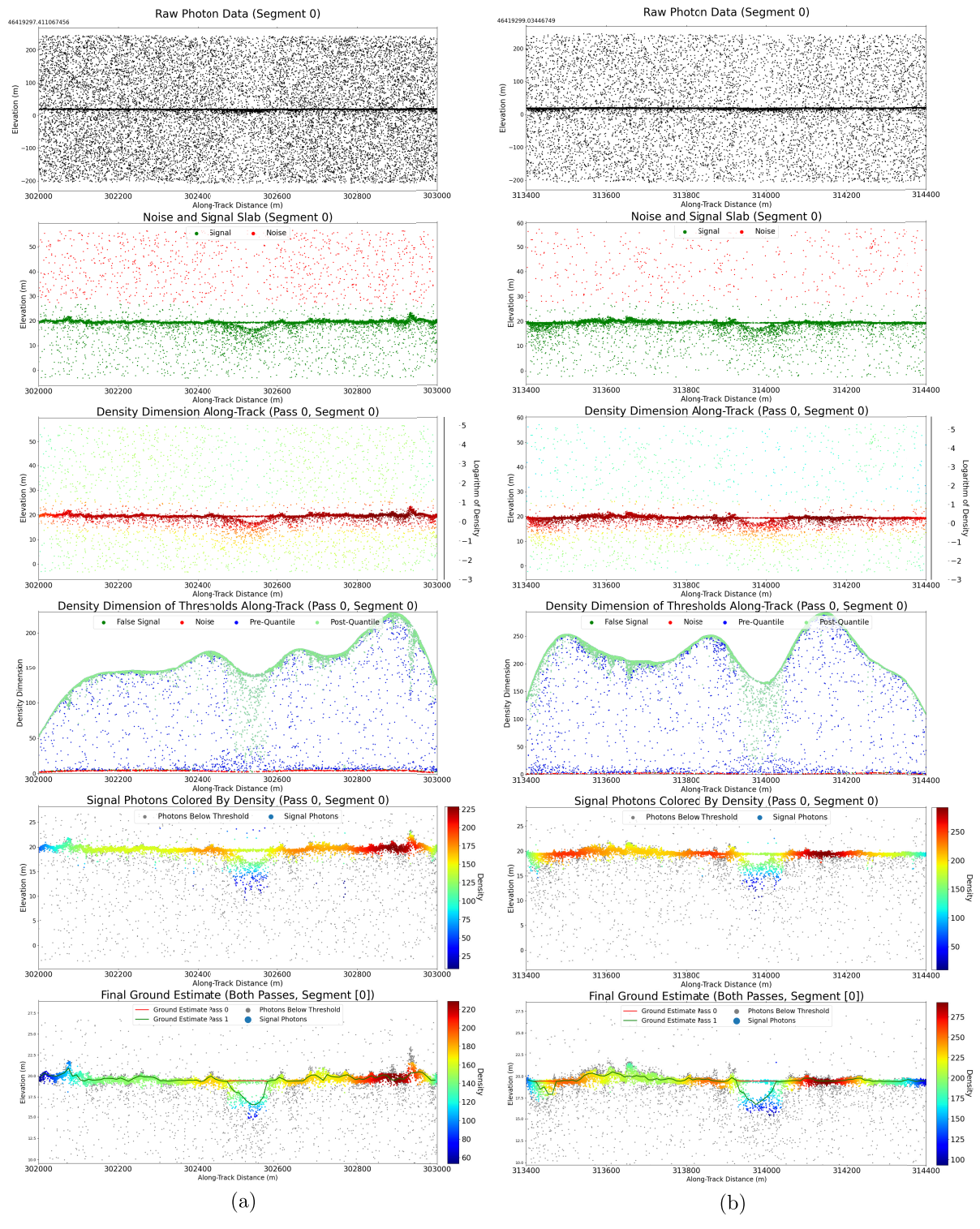


Fig. 2. Megaplots illustrating the steps of the DDA-bif-seaice. (a) 1298_gt31_82.637.png – gt3l outer beam, strong [mega 1]; (b) 1298_gt2l_82.727.png – gt2l, center beam, strong [mega 2]. Granule information in caption of Fig. 1.

steps already detailed for the DDA-ice-1 in Section IV-F are simply summarized. New algorithms steps specific to the DDA-bif-seaice are introduced here.

Algorithm steps of the DDA-bif-seaice are illustrated in Fig. 2. There, four examples are given to provide insights into the operation of the algorithm steps for different seaice environments, reflection situations, and morphological

complexities and for an outer beam (strong beam 3) compared with the near-nadir central beam (strong beam 2).

(Step 1) Large-scale separation of signal and noise slabs:

The input to this step is the set of raw ICESat-2 ATLAS photons, also called the photon point cloud, seen in Fig. 2 (x - 1), where x = a, b, c, d. The signal of the Earth's

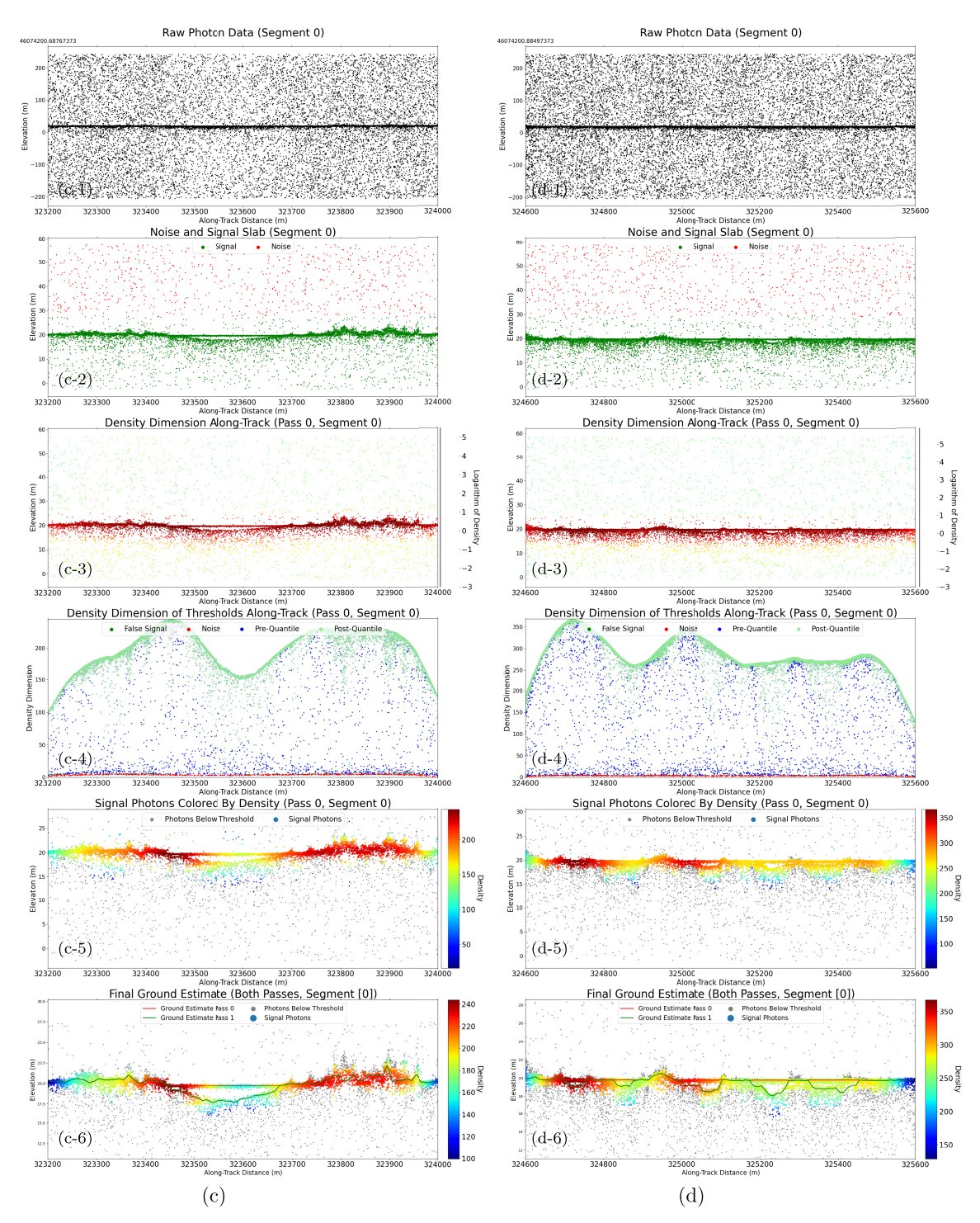


Fig. 2. (Continued.) Megaplots illustrating the steps of the DDA-bif-seaice. (c) 1237_gt31_82.818.png – gt3l outer beam, strong [mega 3]; large pond with variable density (d) 1237_gt31_82.831.png – gt3l, outer beam, strong [mega 4]. Granule info in caption of Fig. 1.

surface, where the surface of sea ice, sea water, or pond water, coincides with the height range of the strongest reflectors. The separation of noise and signal slabs at large spatial scales is relatively robust and can be carried out using histograms. The result is shown in Fig. 2 (x-2).

(Step 2) Calculation of the density field using the radial basis function, rbf, for the signal slab and the noise slab (the same as DDA-ice-1).

The density field is shown in Fig. 2 (x - 3).

(Step 3) Operation of an autoadaptive threshold function to separate noise and signal photons, using density as an additional dimension.

At this point, the same threshold algorithm is run as in the DDA-ice-1, but with a lower quantile, currently q=0.15 (see the table of algorithm-specific parameters, Table I), that passes more photons as candidates for examination in the following steps. Running the autoadaptive threshold function creates a set of signal photons, denoted by \mathcal{S} (14). Note that \mathcal{S} is a

subset of the set of photons in the signal slab (for DDA-ice-1 and DDA-bifurcate-seaice). With the lower quantile, the set $\mathcal S$ is not the set of ice-surface photons anymore, but rather a set of photons, which are candidates for melt-pond surface or bottom photons. Running the original threshold algorithm with a really low threshold serves to eliminate outlier photons. We call the resultant set the presignal set. The main thresholding will be applied at a later step in the melt-pond algorithm of the DDA-bifurcate-seaice (see Step 4).

The operation of the autoadaptive threshold function for the presignal set is illustrated in Fig. 2 (x-4), with the resultant presignal set shown in Fig. 2 (x-5).

(Step 4) Melt-Pond Detection: Bifurcation algorithm with additional autoadaptive thresholding.

The actual melt-pond detection comprises several steps. The result of these steps is shown in Fig. 2 (x - 6). Building on the logic of the thresholding algorithm (Step 3), a new bifurcation algorithm with additional autoadaptive thresholding is designed. The new algorithm for melt-pond detection is implemented in a function called *compute_threshold_melt_pond*, abbreviated as *ctmp*, applied to signal photons only, i.e., to photons in the set S that results from Step 3. Note that *ctmp* is not applied to all photons in the signal slab, only to signal photons resultant from Step 3. The function *ctmp* currently uses the same quantile, q, as the thresholding in Step 3 (i.e., q = 0.15.)

The function returns the photon signal sets associated with the top surface and the bottom surface (if applicable); these are subsets of the presignal set from Step 3. In case only one surface is found, the result is identical to that of the DDA-ice-1 (with appropriate parameters).

(Step 4.1a) ctmp-1a: Calculate a vertical histogram of the signal photons.

The bifurcation code begins by determining if two surfaces exist. A vertical histogram is calculated for the photons in the set S (at vertical resolution mp_bin $_v$), for every segment of a horizontal resolution mp_bin $_h$. Here, we use mp_bin $_v = 0.1$ and mp_bin $_h = 25$ (units in meters). All following steps are carried out for each horizontal step of resolution mp_bin $_h$.

(Step 4.1b) ctmp-1b: Apply a binomial filter to the histogram.

Then, the histogram, H, is filtered (or smoothed) using the Butterworth filter. In this simple form, it is a binomial filter. The new histogram counts H_{new} at vertical location x (or elevation), are given the value

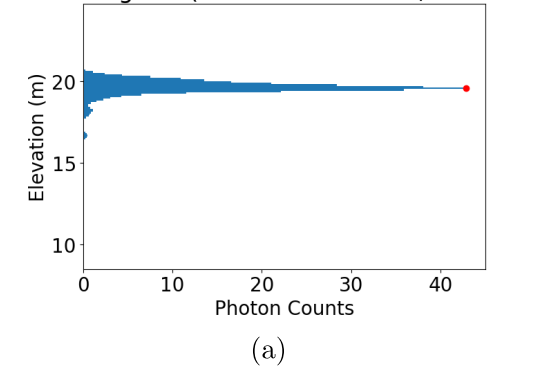
$$H_{\text{new}}(x) = H(x-2) \cdot 0.0625 + H(x-1) \cdot 0.25 + H(x) \cdot 0.375 + H(x+1) \cdot 0.25 + H(x+2) \cdot 0.0625.$$
 (15)

For edge cases, one simply drops the term that is out of bounds. For example, for bin 0, we use

$$H_{\text{new}}(0) = H(0) \cdot 0.375 + H(1) \cdot 0.25 + H(2) \cdot 0.0625.$$
 (16)

(Step 4.2) ctmp-2: Find peaks in the filtered vertical histogram of signal photons.

Vertical Histogram (Start: 302425.0 m, width: 25.0 m)



Vertical Histogram (Start: 302525.0 m, width: 25.0 m)

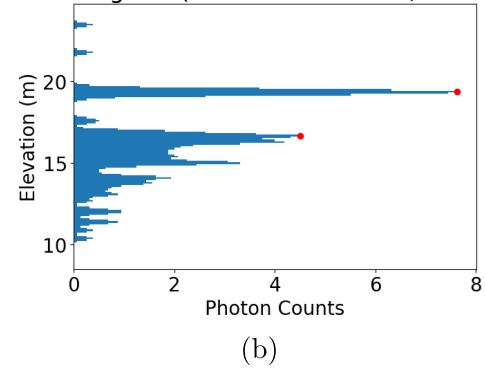


Fig. 3. Histograms illustrating bifurcation criterion in the DDA-bif-seaice submodule ctmp (steps 4.1 and 4.2). (a) Histogram (filtered) typical of a single surface. (b) Histogram (filtered) typical of a melt pond. Histograms stem from example 1298_gt3l_82.637.png, shown in Figs. 1(e) and 2(a). – gt3l outer beam, strong. Example from ICESat-2 ATLAS granule ATL03_20190618062235_12370304_005_01.h5, RGT 1237, collected June 18, 2019, ICESat-2 ASAS version 5 dataset.

Peaks in the filtered vertical histogram will indicate reflectors, and if there is more than one reflector, a melt-pond may exist in the examined location. The determination of peak locations is currently implemented as a call to the *scipy* library function $find_peaks$, which is called with the maximum number of peaks set to 2. There are two cases possible: 1) if at least two peaks are found, then set $peak_1 = top$ and $peak_2 = bottom$ and apply the algorithm for the bifurcation case and 2) if only one peak is found, then only one surface is identified. The *scipy* function also determines a saddle point (a minimum between the two peaks). The two cases of peak determination are illustrated in typically filtered histograms in Fig. 3; such histograms can be output by the DDA-bif-seaice as an option.

1) If at least two peaks are found, then the algorithm finds the two largest peaks, where *pk*1 is the bin associated with the top surface and *pk*2 is the bin associated with the bottom surface. Next, we find a specific histogram range, or a signal "slab," for each peak (or associated surface). We first find the minimum histogram bin between the two peaks *pk_min*, referred to as the saddle point. The number of bins, or distance, between the saddle point and the peak for the top surface, is called *d*. The slab associated with the higher surface

(top surface) is bounded below by the saddle bin and above by pk1 + d. Thus, the upper slab is centered at the peak pk1 with a size determined by the separation of the peak bin from the saddle point bin between the two peaks. If the upper boundary is above the histogram limit, then the top of the slab boundary is set to the uppermost histogram bin. The second slab, associated with the lower surface, ranges from the saddle bin pk_min to the first bin below the second peak pk2 that drops to 0 signal photon counts. In this case of two identified surfaces (case 1), the function returns the two-photon signal sets associated with the top and bottom surface, using S_{top} to denote the set of the top (surface) photons and S_{bot} to denote the set of bottom photons.

The determination of the peaks utilizes the following values (see Table I). The count of a minimal peak in the histograms is set as M=3 photons, and the minimal prominence of a peak above the saddle is set as D=3 photons, applied to the filtered histogram; i.e., a peak must at least have three photons and be at least three photons above the saddle point in the filtered histogram. These are algorithm-specific, tunable parameters. In addition, minimal pond depth is set to be 0.5 m, a constraint that is associated with the 1.5-ns pulsewidth of the ATLAS sensor (1.5 ns equals 0.45 m at the speed of light).

As a result, each photon that has been identified as a signal photon is associated with one of the classes of pond bottom or pond surface for a ponded area. Up to this point in the algorithm, all operations are carried out per photon, and in consequence, the nominal 0.7-m along-track resolution (point spacing) of the ATL03 data is retained in the pond detection. The regular ground follower is then applied in a modified version to both signal sets S_{top} and S_{bot} to interpolate the two distinct surfaces (for each along-track bin). Note that in the code the ground follower is applied to the union of all the along-track bins, i.e., the entire track, all at once. It uses the same quantile dq = 0.75 for both surfaces. The modified ground follower is described in (Step 5).

2) There is also the case where only a single surface is identified (one peak returned from the *find_peaks* function with our parameterization). In this case, the threshold function acts as for DDA-ice-1 to return the thresholded photons to be interpolated by the ground follower. The code simply returns the same thresholded set of photons as the photon signal slab for both the top and bottom surfaces, which implies that the two surfaces would merge in the ground follower (Step 5); formally, the same ground estimate is output for both surfaces for this particular horizontal or along-track bin. The ground follower is described in (Step 5) for this case as well.

(Step 4.3) ctmp-3: Create a set of bifurcation and rejoining points: a counter for discrete ponds.

In this step, a set of bifurcation points and a set of rejoining points are created, which aid in keeping track of the start and end locations of discrete ponds. This set is later examined in the melt-pond ground follower, which has the capability to function for pond regions and regions of a single surface. Numerically, the identification of bifurcation and rejoining points is carried out as part of (Step 4.2), changing the value of an indicator whenever a switch in the number of peaks occurs.

As a result of this step, we are able to carry out analyses of properties per pond, such as maximal and average pond depth and pond width.

(Step 5) Pond-specific surface follower.

In Step 5, a melt-pond specific surface follower is applied to both the top surface signal-photon set, S_{top} , set and the bottom surface signal-photon set, S_{bot} . The surface follower employs the same roughness-adaptive ground follower function, as described for the DDA-ice-1. Numerically, the ground-follower algorithm moves along track, calculating surface heights for each segment for both surface sets. The melt-pond ground follower uses a melt-pond quantile, dq =0.75. The role of the melt-pond quantile in the ground follower function is to "place" the reflector/ground height at a certain percentile of the set of signal photons in the respective set (the set of surface signal photons or the set of bottom signal photons). In the current code version, the same melt-pond quantile dq = 0.75, is applied for both surfaces, but different quantiles could be used in a future version of the algorithm. There is also an option to place surface height at max density, which is not used in the current melt-pond analysis.

The same values of the ground-follower resolution, $R = 10 \ [m]$, and the reduction factor for rough surfaces, r = 2, are employed for both surfaces, but one can be smooth (resulting in the 10-m resolution) and the other one can be rough (resulting in the 5-m resolution). Typically, the pond bottom is rougher than the pond surface, but we do not force the pond surface to be flat at this point (because the top surface could also be a ridged surface between ponds).

The result of the surface follower is a set of piecewise linearly interpolated surface heights, $S_{top\text{-}interp}$, and piecewise linearly interpolated bottom heights, $S_{bot\text{-}interp}$.

Case 2: In case (2) (no pond), the algorithm works as follows: if no pond is detected (and between ponds, i.e., wherever only one surface exists), then the roughness-adaptive ground follower is applied, as described in Step 4 of the DDA-ice-1. This capacity creates a surface that follows ridges (rough sea-ice areas) with a smaller segmentation in the piecewise ground follower, as well as smooth sea ice, where a larger segmentation is used (see Table I). The result of the surface follower is a set of piecewise linearly interpolated surface heights, $S_{top-interp}$.

In case (1) (pond), an additional algorithm module for correction of melt-pond surface heights is applied (Step 6). Technically, to avoid edge effects in the ground follower between case 1 (two surfaces) and case 2 (single surface), the surface is duplicated into two identical sets for case 2.

(Step 6) Correction of melt-pond surface heights and calculation of pond statistics.

(Step 6.1) Correction of melt-pond surface heights.

Case 1: In case (1) (pond), the surface follower.

- 1) Makes the top surface flat and horizontal.
- 2) Throws out false negatives.

For case (1), the following steps are carried out. This is implemented as running a "for" loop over the ponds, and the following steps are carried out for each pond.

(Case 1.1): If the mean elevation of the surface is larger than the elevation of the pond edges plus a small value ϵ , then it is determined that de facto no pond exists: calculate m(s) as the mean of the surface height for the top of the pond, based on the heights of the photons in the top surface signal slab, and calculate the edge average as $a(e) = h((left_edge) + h(right_edge))/2$. Then apply the following criterion, if:

$$m(s) > a(e) + \epsilon$$
 (17)

then set top = bot.

This throws out false positives created by too small height differences.

Current value is $\epsilon = 0.2$ m.

(Case 1.2): If the two pond edges are very different in height, the set top = bot.

Current code uses

$$|h(left_edge) - h(right_edge)| > 1.$$
 (18)

This step throws out false positives created by ridge edges. (Case 1.3): Min-width criterion: a minimum-width criterion is applied to map ponds. This requires that a least three depth measurements are taken, i.e., the pond needs to have a minimal size of three segments of the ground follower.

Based on the ground follower resolution, the minimal pond size is 30 m for smooth surfaces, if the length of piecewise linear interpolator size is 10 m (see Table I). Using R=2 for the ratio of smooth to rough segment lengths in the ground follower, the minimal pond size that is mapped is 15 m. That means, if the bottom is rough then we can find ponds of 15-m minimal size.

This can be interpreted as follows: if a pond formed on really rough ice and melting started and the sea-ice morphology was approximately preserved during subsiding, leading to rough pond bottoms, then we can identify 15-m wide ponds. Notably, the along-track bin size of the ground follower can be smaller than the horizontal bin size of the bifurcation algorithm, because Step 5 is applied to the signal photons in the bottom and top signal slabs.

(Step 6.2) Calculation of pond statistics.

As the algorithm steps through the set of ponds, statistical values of interest to sea-ice scientists are calculated. These include the following.

- 1) Pond width.
- 2) Maximal pond depth.
- 3) Average pond depth.

Values of maximal and average pond depth are not corrected for the lower speed of light in water, compared with the speed of light in air. Atmospheric corrections on the ATL03 product account for the slightly lower speed of light in air, compared with the speed of light (in vacuum), see [32].

(Step 6.3) Correction for speed of light in water.

As an approximation, the range between the pond surface and the pond bottom can be multiplied by 1.3. (Water has a refractive index of 1.3, whereas the refractive index of vacuum

is 1.0). This correction is currently applied outside of the DDA-bif-seaice in the postprocessing of pond depths.

Results of the pond statistics are utilized in the companion paper on the evolution of melt ponding on Arctic seaice in the multiyear seaice region, including the Lincoln Sea (see Section V and [5]).

V. APPLICATION: MELT-POND DETECTION IN ICESAT-2 ATLAS DATA FROM THE MULTIYEAR ARCTIC SEA-ICE REGION

The DDA-bif-seaice was applied to ICESat-2 ATLAS data from the multiyear Arctic sea-ice region [multiyear Arctic sea-ice region (MYASIR); Fig. 4] for the melting seasons (June-August) of 2019 and 2020. In the Central Arctic, early melt onset and melt onset occurred on the 3rd and 16th of June 2020, respectively (cf. [28]). We conclude the study in August, as imagery of the region shows freeze conditions and a pond with a frozen surface is no longer penetrable by the laser. The study region and time period are described in more detail in [5]. Results from 2019 are given in Fig. 1 and already discussed in Section III, focusing on the illustration of pond detection capabilities: 1) in different beams; 2) in different sea-ice environments; and 3) in various situations of background and signal strength. Now that the algorithm has been introduced, we take a closer look at examples that illuminate certain typical sea-ice morphological situations and problems of pond detection.

A. Ponds Among Ridges and in Complex Sea-Ice Topography

A frequently occurring morphological type of sea ice is that of faulted ice blocks. These form when compressive stress is applied to a sea-ice province, for example by wind, causing fracturing of the sea ice into blocks, which are then thrust upward and can be partly pushed on top of each other. Melt ponds tend to form on the side of a faulted block. Detection of ponds aside from fault blocks may provide useful information for modeling sea-ice physical processes at high resolution.

The example in Fig. 5(a) shows two ponds, which have surfaces at different heights and the two ponds are forming in two of the typical, but different, neighboring environments: pond 1 (at 4400) is located among of sea ice with a low topographic relief, which is relatively smooth to the left of pond 1 and somewhat ridged on the right of pond 1. A small fault block could be located immediately right of pond 1. Pond 2 (at 4600) is situated to the side of a fault block, where the fault block forms a ridge.

The surface follower is not optimized to follow the ridge topography in this code version (DDA-ice v18.0, December 2021), resulting in unrealistically smoothed-out topography [Fig. 5(a)]. Analysis of ridged and ponded areas with an older code version (DDA-ice v16.0, October 2021), which includes a different surface follower for single surfaces, renders ridge topography more realistically [Fig. 5(b)].

B. Results From Summer 2020 Data

For the 2019 data, analysis was carried out automatically detecting ponds, which were already detected manually as well

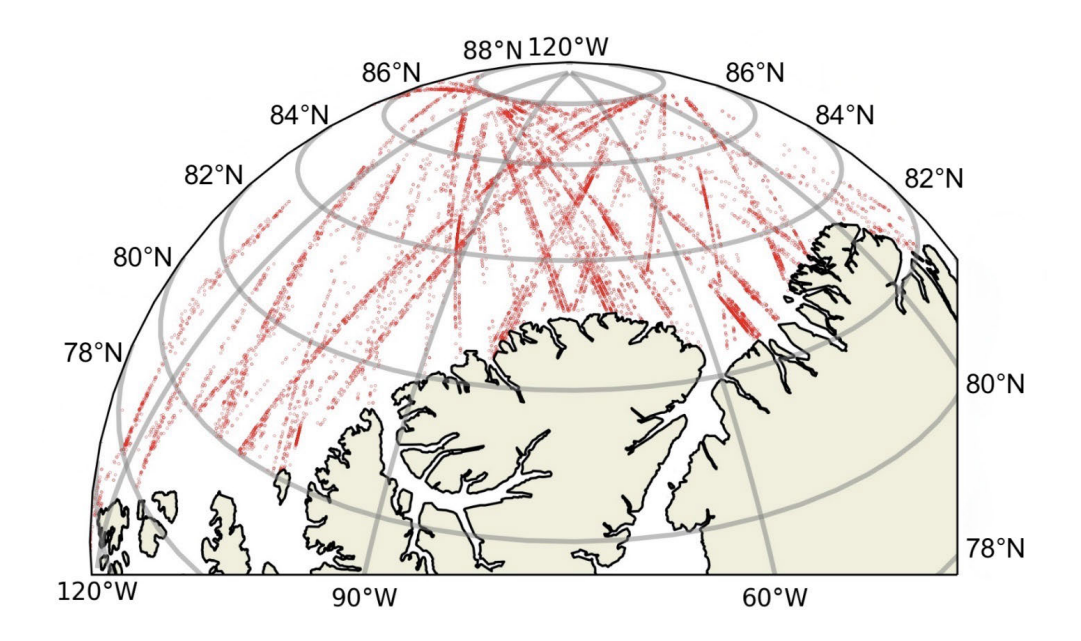


Fig. 4. Location of melt ponds detected by the DDA-bif-seaice in the study area, the MYASIR, for summer 2020. Each small red circle indicates a melt pond detected with the DDA-bif-seaice, a total of approximately 10 200 ponds are shown. Note that DDA-bif-seaice was run over about 10% of ICESat-2 tracks, outer strong beams.

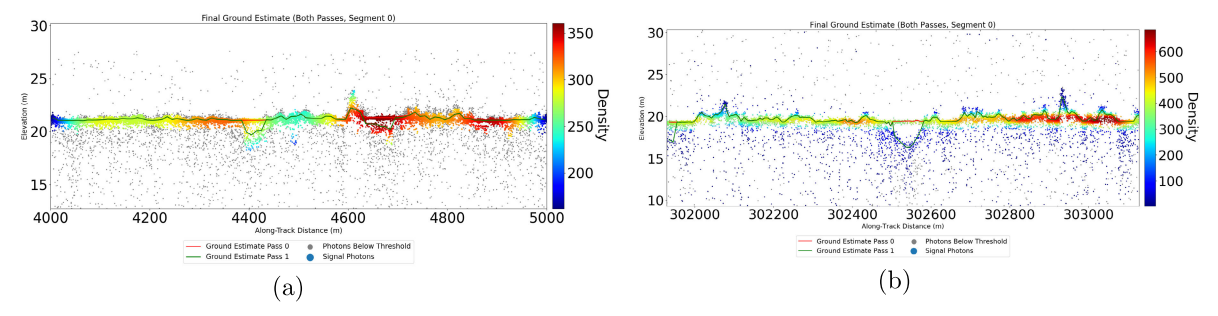


Fig. 5. Automated detection of melt-ponds on sea ice among ridges and complex surfaces with the DDA-bifurcate-seaice. ICESat-2 data from the Lincoln Sea. (a) Example from ICESat-2 ATLAS granule ATL03 20200628121109 00480804 005 01.h5, RGT 48, collected 2020-June-28, ICESat-2 ASAS version 5 data set. Strong outer beam gt11. Example of two ponds with different different surface heights in complex sea-ice environments. pond 1 (at 4400), pond 2 (at 4600), artifact avoided at 4850. Ground follower not optimized for ridge topography (2020 data, seg0). (b) Application of DDA-bif-seaice (v.16.0) with surface follower for single surfaces optimized to adapt to rough surfaces, such as ridge topography, between ponds. Examples from ICESat-2 ATLAS granule ATL03 20190618062235 12370304 003 01.h5, reference ground track (RGT) 1237, collected 2019-June-18, ICESat-2 ASAS version 3 data set (2019 data, 1298 gt31 82.637.png). The same example as Fig. 1(e).

as with the UMD MPA to provide a proof of concept. The UMD algorithm requires visual determination of pond location (thus, ponds have pond identifiers in the file names and these are utilized in comparisons of results from the two algorithms and in the examples in Fig. 1). The DDA-bif-seaice was applied to the same ATLAS tracks, without giving information on pond location to the algorithm, and pond existence and location were determined fully automatically.

For the 2020 data, a large set of tracks (10% of all tracks collected) was processed for a large area of the Arctic, using only strong-beam data. Results from July 13, 2020 data (Fig. 6) show ponds at different stages of formation and in different sea-ice environments, some of which are province types not previously illustrated in Fig. 1. Notably, total signal strength in examples Fig. 6(a)–(e) is significantly lower than in the 2019 examples presented, but higher for the examples in Fig. 7. The analysis for all 2019 and 2020 data was

run using DDA-ice v18.0 with the same algorithm-specific parameter sets, given in Table I, which further demonstrates the autoadaptive capability of the algorithm. In Fig. 1(h), a large pond neighbors small ponds that are correctly detected, as well as a region of dead-time effects that are appropriately avoided.

Examples include the following: 1) a pond at an early stage of formation, located in a smooth sea-ice area [Fig. 6(a)]. Neighboring areas show the penetration of ice with water, likely leading up to pond formation; 2) ponds among ridges at various formation stages [Fig. 6(b)]; 3) a pond in a partly ridged, partly smooth area [Fig. 6(c)]; 4) a pond in a typical location near a ridge [Fig. 6(d)], as already described in Section V-A; 5) an unusually small pond at an early formation stage [Fig. 5(e)]; 6) a small pond that is detected. Notably, no false positives are detected in a high-density area between 665 600 and 665 800 (see Section V-C); and 7) an unusually

Authorized licensed use limited to: UNIVERSITY OF COLORADO. Downloaded on June 09,2023 at 22:19:57 UTC from IEEE Xplore. Restrictions apply.

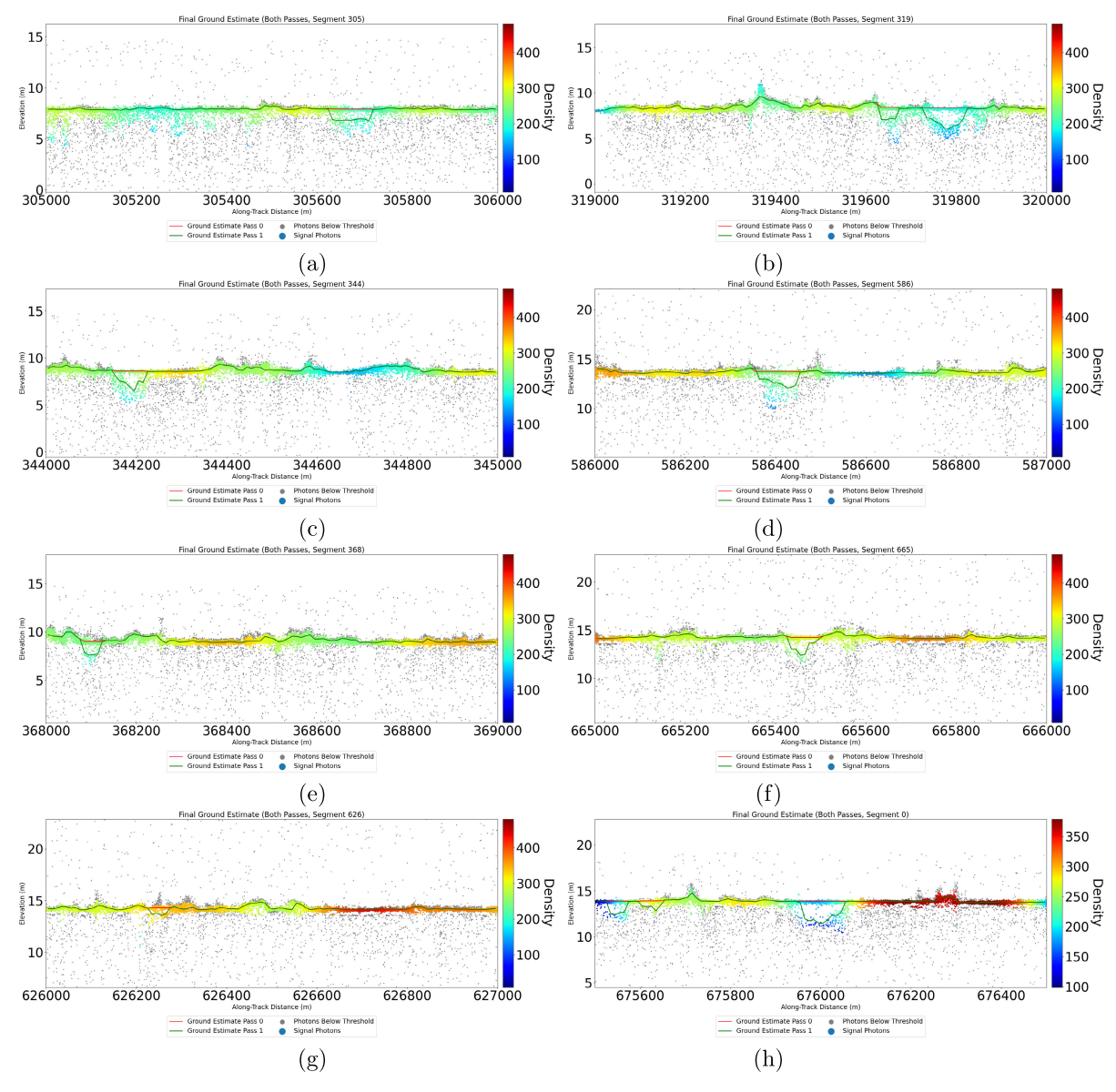


Fig. 6. Examples of ponds detected with the DDA-bif-seaice in summer 2020 ICESat-2 ATLAS data, Multi-year Arctic sea-ice region. Examples of ponds are from ICESat-2 ATLAS granule 20200713151204 02790804 005 01 gt11 strong outer beam, reference ground track (RGT) 279, collected 2020-July-13, ICESat-2 ASAS version 5 data set. (a) Pond in the making, located in smooth sea-ice area. Neighboring areas show penetration of ice with water, likely leading up to pond formation (2020 data/0713, seg305). (b) Ponds among ridges area, various formation stages. Surface follower not optimized for ridge topography in the code version (2020 data/0713, seg319). (c) Pond in partly ridged, partly smooth area (2020 data/0713, seg344). (d) Pond in typical location near a ridge (2020 data/0713, seg586). (e) Small pond detected (2020 data/0713, seg368). (f) Small pond detected. no false positive detected in high-density area between 665600 and 665800 (2020 data/0713, seg665). (g) DDA avoids dead-time effects (seen as high-density regions below the surface and parallel to the surface. Here, three levels.). Thus DDA avoids false positives (2020 data/0713, seg526). (h) Large pond detected at 676000. Small ponds detected near 675600. Avoidance of saturation effects in regions of high surface reectance (density 350 or larger) (2020 data/0713, seg675 and 676).

deep pond (approximately 4-m uncorrected depth and corresponding to 5.2-m corrected depth), that is situated between two small ponds (near 675 600) and a region of high surface reflectance (density 350 or larger).

A physical interpretation of melt-pond evolution based on the results from analysis of large datasets over the MYASIR with the DDA-bif-seaice is given in [5].

C. Avoidance of Saturated Signals

In situations of highly reflective sea-ice surfaces, the lidar signal received by the ATLAS sensor can become saturated. This means that more photons are received than can be

counted. As a result, a second range bin of photons will appear at a fixed range, or distance, determined by the detector dead time. The first of these is 0.43 m below the saturated surface. For the central beam pair, whose beams are near-nadir pointing at the ice surface, saturation is relatively common over specular refrozen ponds or specular water surfaces of melt ponds. This effect creates a challenge in possible misclassification of saturation effects as melt ponds because the range of 0.43 m lies within the depth range of melt ponds. The dead-time effect leads to signals that are a fixed distance below the height of the primary surface and follows the shape of the primary surface. For pond surfaces, which are flat, the artifact

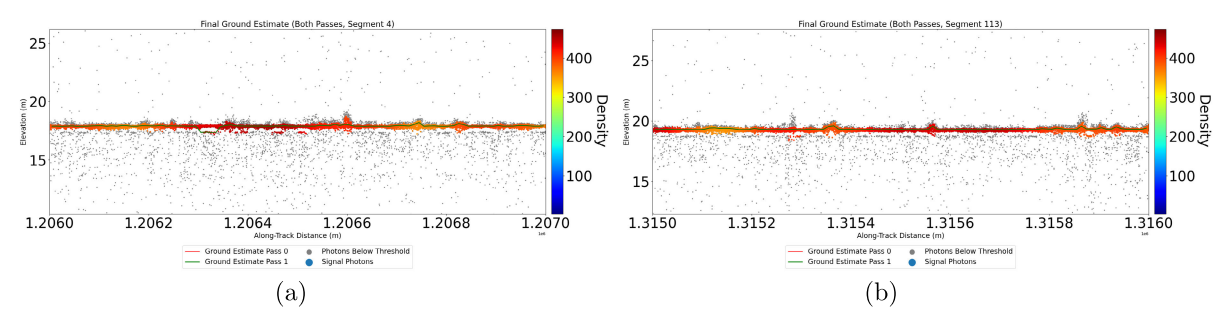


Fig. 7. Avoidance of false positives in DDA-bif-seaice pond detection in highly saturated 2020 ICESat-2 ATLAS sea-ice signals, Multi-year Arctic sea-ice region. Examples of ponds are from ICESat-2 ATLAS granule 20200803013027 05910804 005 01 gt11 strong outer beam, reference ground track (RGT) 591, collected 2020-August-3, ICESat-2 ASAS version 5 data set. (a) A false positive pond identification (between 1.2064 and 1.2066) (2020 data/0803, seg4). (b) All false positives are avoided in this segment of dominated by saturated signals (2020 data/0803, seg113).

surface is also flat [see Fig. 7(b)]. The dead-time effect can be persistent over long distances of the ICESat-2 ground tracks [see Fig. 7(a) and (b)].

The DDA-ice-1 has the property to avoid secondary signals in most situations, simply because those are less dense than the primary surface. For the DDA-bif-seaice, the challenge is larger, because the goal is now to detect secondary surfaces that are weaker. In many cases, detection of false positives, misidentified as ponds, is avoided by the *cmtp* module of the algorithm, as illustrated in Fig. 6(f) (between 665 600 and 665 800) and Fig. 6(g) (between 626 600 and 626 800). However, avoidance of misclassification of dead-time effect-generated secondary surfaces as false ponds is far from perfect, as seen in the example in Fig. 7(a) between 1.2064 and 1.2066, among, otherwise, correctly avoided secondary signals, while Fig. 7(b) gives an example of a strong saturation effect (density 400).

Data situations, such as seen in Fig. 1(d), may benefit from a validation campaign (see Section VII), to distinguish between sections that may be dominated by saturation (dead-time effect), while the ponds in Fig. 1(c) and (f) have complex bottom topographies, and thus, are not saturation (dead-time) artifacts, despite the strong surface reflectance (density values of 200–250). Notably, the absolute density value is not a well-defined criterion for saturation, because the density value depends on the algorithm-specific parameters that control the kernel as well as on background intensity and because the threshold function is autoadaptive.

An experimental algorithm to avoid saturation effects is in development, but not applied here. Because of the saturation problem, the analysis in [5] utilizes only results from the outer beams, pairs 1 and 3. Furthermore, the analysis in [5] was restricted to strong beams, because only a subset of all ICESat-2 tracks crossing the multi-year Arctic sea-ice region could be processed due to constraints of computer time on ADAPT and detection capability is better for strong beams than for weak beams in general.

The ATL03 product has flags for "saturated" and "near-saturated" signals, preliminary analysis indicates that these flags do not correlate well with saturation effects and do not provide a good solution for the saturation problem.

VI. EVALUATION: COMPARISON WITH RESULTS FROM ATLO7 AND FROM THE UMD MELT-POND ALGORITHM

A. Comparison With ICESat-2 ATLAS Sea-Ice Product ATL07

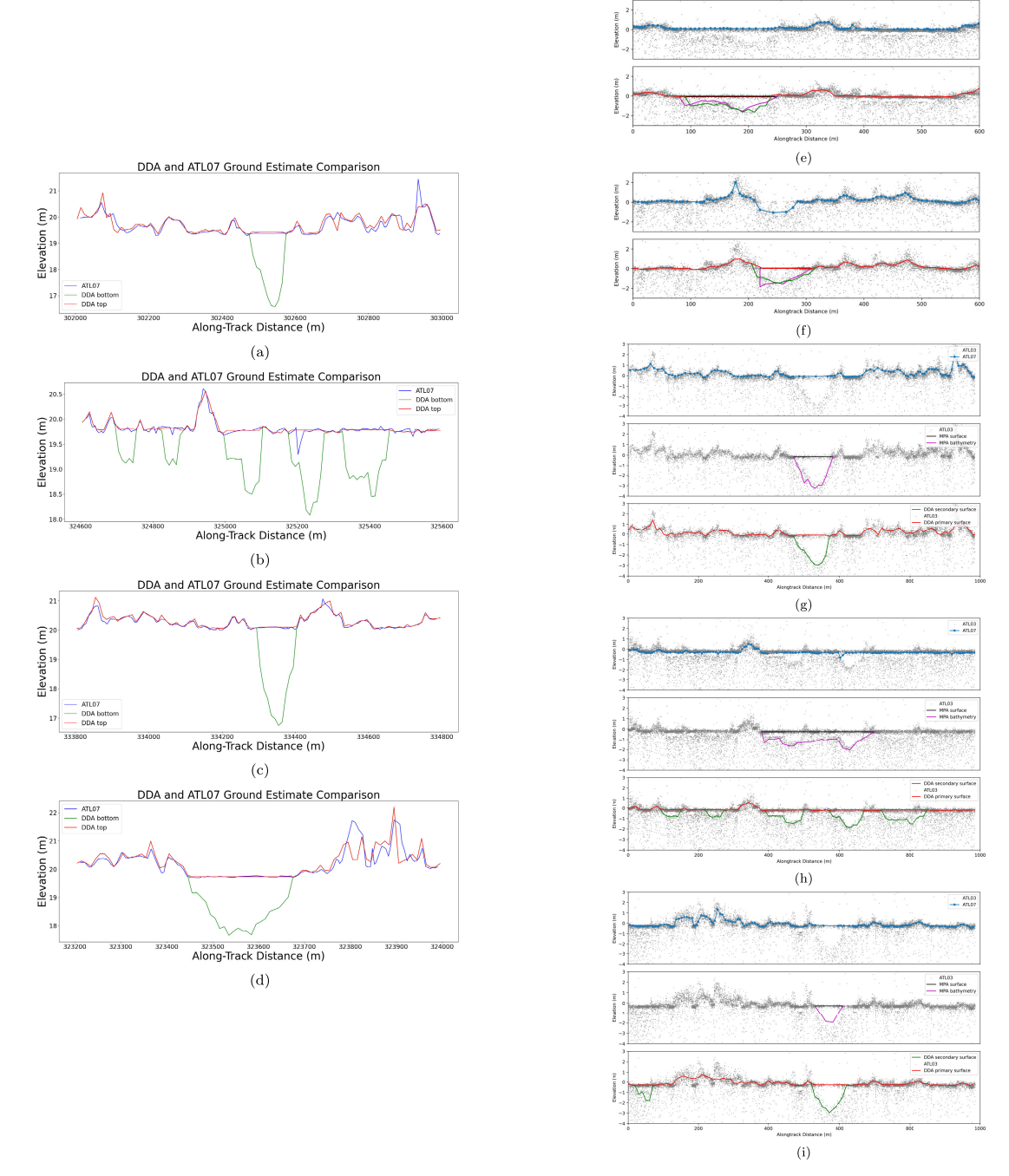
The ICESat-2 ATLAS sea-ice product ATL07 is not designed to detect two surfaces; hence, melt ponds are not reported and in ponded regions, the surface height on ATL07 may represent that of the surface or a value between the surface and the pond bottom [6]. A few examples showing the information gain between ATL07 and results from the DDA-bif-seaice are given in Fig. 8. The results suggest the inclusion of melt-pond information in a future version of the ICESat-2 ATLAS products.

In regions without melt ponds, surface heights of ATL07 and from the DDA-bif-seaice are in good agreement, where surface topography is smooth or moderately rough; however, in ridged areas, the DDA ground follower needs to be revisited to better reflect high topographic relief (see Fig. 5).

B. Comparison to Melt-Pond Depth Measurements Using the UMD Algorithm

In addition to the visual interpretation of the photon cloud, results from several hundred manually identified ponds from the 2019 melt season were employed for evaluation of the DDA-bif-seaice results during the early stages of algorithm development (Fig. 8). The 2019 data analyses were rerun with the latest DDA algorithm version (v18.0) for inclusion in this article. Ponds were visually identified in ICESat-2 ATLAS photon cloud data (ATL03 data) and computationally analyzed using the UMD MPA. To facilitate a study of the evolution of melt ponds across the entire MYASIR, a representative subset (10%) of all ICESat-2 ATLAS data collected in this region in the summer of 2020 (June–August) was analyzed with the DDA-bif-seaice. The 2020 data analysis supports a statistical comparison of results from the two algorithms (Fig. 9).

1) Description of the University of Maryland Melt-Pond Algorithm: The UMD MPA is a computational algorithm for the detection of melt ponds in ICESat-2 ATLAS (ATL03) data that requires a priori determination of the location where a pond exists, then centers the pond analysis on the middle of the pond and computes the depth of the pond in increments. Control points at the pond bottom can be added. The MPA is



Comparison of pond detection with the DDA-bif-seaice and UMD MPA to results on ICESat-2 ATLAS sea-ice product ATL07. (a)-(d) Comparison of pond detection with the DDA-bif-seaice to results on ICESat-2 ATLAS sea-ice product ATL07. Blue—ATL07, red—DDA-bif-seaice surface heights, and green—DDA-bif-seaice pond bottom heights. Examples in (a) and (c) are from ICESat-2 ATLAS granule ATL03_20190618062235_12370304_005_01.h5, RGT 1237, collected June 18, 2019, ICESat-2 ASAS version 5 dataset. Examples in (b) and (d) are from ICESat-2 ATLAS granule ATL03_20190622061415_12980304_005_01.h5, RGT 1298, collected June 22, 2019, ICESat-2 ASAS version 5 dataset. (a) 2019: 1298_gt31_82.637 [see Fig. 1(e)]. (b) 2019: 1237_gt31_82.831 [see Fig. 1(d)]. (c) 2019: 1298_gt31_82.911 [see Fig. 1(f)]. (d) 2019: 1237_gt31_82.818 [see Fig. 1(a)]. (e)-(i) Comparison of pond detection with the DDA-bif-seaice and the UMD MPA to results reported on ICESat-2 ATLAS sea-ice product ATL07. (e) and (f) 2020 data. Top panels in (a) and (b): ATL07 (blue). Bottom panels in (a) and (b): green—DDA-bif-seaice pond bottom, magenta—UMD MPA pond bottom, and red—DDA-bif-seaice surface of ponds and between ponds. (a) and (b) From Buckley et al. [2]. (e) Example where ATL07 follows the pond surface. Examples in (e) are from ICESat-2 ATLAS granule ATL03_20200628055359_00440804_005_01.h5, RGT 44, strong outer beam gt3l, collected June 28, 2020, ICESat-2 ASAS version 5 dataset. start_dt 78559154.55 and stop_dt 78559154.71. (f) Example where ATL07 follows the pond bottom. Examples in (f) are from ICESat-2 ATLAS granule ATL03_20200701061119_00900804_005_01.h5, RGT 90, strong outer beam gt3l, collected July 01, 2020, ICESat-2 ASAS version 5 dataset. start_dt 78819350.67 and stop_dt 78819350.84 (g, h, i): 2019 data. Examples in (g) and (i) are from ICESat-2 ATLAS granule ATL03_20190622061415_12980304_005_01.h5, RGT 1298, collected June 22, 2019, ICESat-2 ASAS version 5 dataset. Examples in (h) are from ICESat-2 ATLAS granule ATL03_20190618062235_12370304_005_01.h5, RGT 1237, collected June 18, 2019, ICESat-2 ASAS version 5 dataset. (g) 2019 data: 1298_gt3l_82.637 [see Fig. 1(e)]. (h) 2019: 1237_gt3l_82.831 [see Fig. 1(d)]. (i) 2019: 1298_gt2l_82.727 [see Fig. 1(g)].

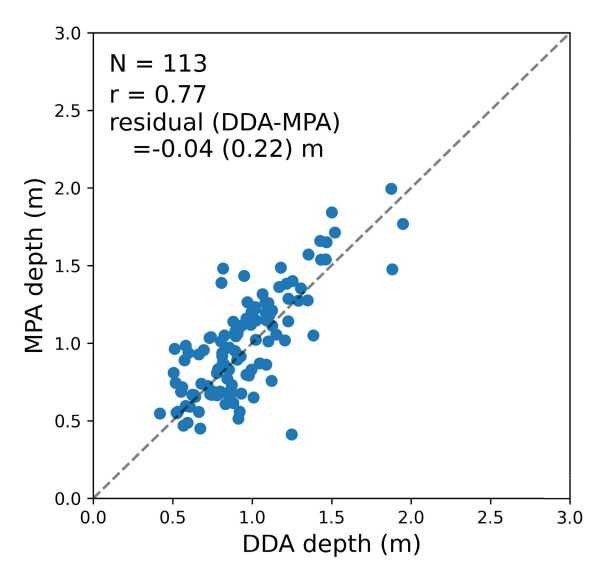


Fig. 9. Scatter plot of mean pond depths for ponds tracked by both the DDA-bif-seaice and the UMD MPA in June and July 2020, 113 ponds total. Residual mean pond depth for DDA-bif-seaice and UMD MPA, calculated as DDA-heights minus MPA-heights.

described in detail in [5] and a brief description is included here. The MPA was developed to track the melt-pond surface and bathymetry in the ATL03 photon cloud. We examined cloud-free areas and manually (visually) identified melt ponds in the photon cloud. In the ATL03 photon cloud, melt ponds present as a level surface, and a bowl-shaped bathymetry with minimal photons return between these two surfaces. We note the start and end of a pond as the point at which the two surfaces become distinguishable. Across the pond, we bin photons into 0.1-m vertical bins and find the surface as the mode of the binned distribution. Next, the photons are binned into 10-m along-track bins and 0.1-m vertical bins. For each 10-m along-track segment, we locate modes below the surface that have at least 5% of the surface photons. The subsurface mode closest to the surface is associated with the reflections from the bottom of the pond and the bathymetry is defined as the vertical bin elevation of this mode. Bathymetry is determined in this way for each of the 10-m along-track segments. To determine melt-pond depth, we subtract the secondary surface that tracks the melt-pond bathymetry from the primary surface that tracks the melt-pond surface. However, the ATL03 algorithm does not account for the change in the speed of light in water when determining the geolocation of the photons. To determine the correct meltpond depth, we multiply the uncorrected depth by the ratio of the speed of light in water to the speed of light in the air (0.749). To increase the along-track resolution, we interpolate the pond depths at 5-m increments.

2) Comparison of Retrieval Results From the MPA and the DDA-Bif-Seaice: To compare results from the two algorithms, the UMD MPA and the DDA-bif-seaice, statistically, we examine retrieved average surface heights and surface widths for the 113 ponds that both algorithms tracked. The statistical analysis utilizes DDA-derived heights resampled at 5-m increments for consistency with MPA-derived heights (rather than average height and width values output by the DDA directly). For each pond, we determine the mean pond depth and plot MPA and

DDA mean pond depth [as seen in Fig. 8(e) and (f)]. We find the algorithms in good agreement, with a correlation value of 0.77, a mean difference of -0.04 m (DDA-MPA; i.e., the bottom height is generally lower in the DDA-bif-seaice results) (Fig. 9). The standard deviation of the residuals is 0.22 m. The difference in depth retrievals between the two algorithms is attributed to the different physical—mathematical philosophies regarding the interaction of light with the cryospheric materials at the bottom of a pond [see, Fig. 8(e) and (f)]; further work on this requires field validation (see Section VII).

The DDA-bif-seaice can detect ponds of a minimal size of a nominal size of 15 m (for rough areas or pond bottoms) and 30 m (for smooth areas or pond bottoms). While these values are algorithm constraints, the detailed analysis of melt-pond evolution in [5] demonstrates that the DDA-bifseaice facilitates the detection of a multiple of the number of ponds compared with the UMD MPA. As seen in Fig. 4, the DDA-bif-seaice detected approximately 10 200 ponds. The statistics of the pond sizes in the referenced study shows that the size range of ponds detected with the DDA-bifseaice is much larger, including large ponds of several hundred meters width as well as ponds of tens of meters width, whereas the MPA finds only large ponds (as may be expected from a manually forced detection). For both algorithms, meltpond size is found to increase as melting progresses early in the season. This again is likely explained by the ability of the DDA-bif-seaice to detect narrow, shallow ponds. The agreement in trends is sufficient to support the physical interpretation of melt-pond processes in the Arctic [5]. Because of the general agreement of pond location and depth trend for the ponds detected in both algorithms, the DDA-bif-seaice has the capabilities expected from a fully automated algorithm for melt-pond detection in ICESat-2 ATLAS data.

VII. DISCUSSION AND OUTLOOK

The DDA-bifurcate-seaice has been successfully applied to the automated detection of ponds and measurement of their depth and extension, as demonstrated in this article and in the applied companion paper [5].

The evaluation of the DDA-bif-seaice in this article has been carried out by application of satellite data analysis and comparison with results from another, also unvalidated, algorithm. Depth determination builds on experience gained in the analysis of water in crevasses, observed during an ICESat-2 airborne validation campaign over the Negribreen Glacier System and on heuristics and sensitivity studies [14]. Systematic differences in pond depth between results from the UMD MPA and the DDA-bif-seaice are attributable to different philosophies applied in the rules for "placing" the surface and pond bottom heights within the photon cloud [5].

Close scrutiny of the four examples of "megaplots" [Fig. 2, threshold function panels (x-4)] shows that large numbers of photons pass in regions of ponds that are characterized by weakly reflecting pond surfaces with clear pond interiors, indicating melt/slush at and below the bottom of the ponds [Fig. 2(a) and (b)]. In contrast, ponds with strongly reflecting surfaces (perhaps refrozen water) have vertically narrower sets of signals at or near the pond bottom, which might indicate a colder, less slushy environment [Fig. 2(c) and (d)]. The

DDA-bif-seaice is controlled by an algorithm-specific set of parameters. The exact optimization of these parameters to identify pond bottom heights within the lower set of signal photons requires validation data from a field campaign. On the other hand, the thought experiments that can be carried out with the mere photon data alone already suggest a wealth of information on the cryomaterials (firn/slush/ice/water) is captured in the ICESat-2 photon data and their density field.

For this article, the algorithm-specific parameter set for the DDA-bif-seaice has been determined by preliminary sensitivity studies, which are a form of mathematical optimization that utilizes iterative steps. Effects of parameter changes on detection and measurement results are analyzed, using a variety of parameters around evolving control parameter sets [12]. This process leaves uncertainties in the depth and width determination of ponds. Actual uncertainties determined in sensitivity studies are on the order of ± 0.2 m, which when integrated over a large part of the Arctic oceans are significant enough to warrant further study. For comparison, an average systematic depth difference of 0.44 m with a standard deviation of 0.22 m was found between results from DDA-bif-seaice and UMD MPA ponds for 113 larger ponds identified by both algorithms in this study. Critical is the penetration of the lidar signal into complex marine cryospheric media, which include, in addition to ice and water, snow on top of the sea ice, snow during metamorphosis, firn, slush, seawater, and brine. As is well-known [47], the penetration depends on frequency. The average ice-surface height difference from red and green lidar data is on the order of 0.15 m (with heights from green laser data generally lower) and standard deviation 0.23 m [12], but specifics depend on the cryomaterials and there are many unknowns. Airborne field data, including red and green lidar data and high-resolution image data, were collected during the ICESat-2 Arctic summer sea-ice campaign in July 2022. These data, once processed and analyzed, may provide constraints for optimization of the algorithm-specific parameter set of the DDA-bif-seaice, and thus, may allow a reduction of uncertainty in depth estimation.

VIII. SUMMARY AND CONCLUSION

The importance of understanding melt processes in the Arctic sea ice in the current realm of climatic warming motivates the development of an advanced mathematical algorithm for the detection of ponds in ICESat-2 ATLAS data. In this article, we introduce the Density-Dimension Algorithm for bifurcating sea-ice reflectors (DDA-bifurcate-seaice or DDA-bif-seaice for short), an algorithm that facilitates automated detection of melt ponds in ICESat-2 ATLAS data, retrieval of two surface heights, pond surface and bottom, and measurements of depth and width of melt ponds.

The ATLAS instrument is the first spaceborne multibeam micropulse photon-counting laser altimeter system, it operates at 532-nm (green light) frequency and registers returns from every single photon in the green-light domain of the sensor. Data are reported in the ICESat-2 ATLAS geolocated photon point cloud product, ATL03. ICESat-2 ATLAS data resolve returns from the top and bottom of melt ponds in the photon point cloud, but because of the high background especially during daylight conditions, separation of noise and signal

and especially detection of two surfaces of typically different intensities are mathematically ill-posed problems.

The DDA-bifurcate-seaice is an autoadaptive algorithm that solves the problem of pond detection at the 0.7-m nominal resolution (received photon spacing) of ATLAS data. In a pond area, each photon identified as the signal is associated with one of the classes of pond surface or pond bottom. The DDA-bif-seaice builds on the Density-Dimension Algorithm for ice surfaces (DDA-ice), utilizing the radial basis function for calculation of a density field and a threshold function that automatically adapts to changes in background, apparent surface reflectance (ASR) and some instrument effects. The centerpiece of the DDA-bif-seaice is a bifurcation module, designed to satisfy the following criteria for a melt-pond algorithm for analysis of point cloud data of lidar data: 1) the algorithm needs to be fully automated (i.e., it should not require a priori information on the existence or location of a pond); 2) detect ponds wherever they exist; 3) avoid false positives; 4) automatically adapt to different background characteristics of daytime and nighttime data and to changes in ASR; 5) find ponds among sea ice of different roughness types (smooth, ridged, and complex); 6) correctly determine the start and end points of a pond along the ICESat-2 ground track; 7) measure the pond depth; and 8) represent the complexity of the sea ice at high resolution. The DDA-bif-seaice includes a ground follower that automatically adapts to the roughness of the pond surface and pond bottom (or of a single surface where no ponds exist). The smallest width of ponds tracked with the ground follower is 15 m for rough surfaces and 30 m for smooth surfaces, currently used height resolution (depth resolution) is 0.1 m. Ponds can be identified in typical locations at the side of ridges formed by fault blocks and in other complex environments. ICESat-2 has been found to penetrate shallow water to 15 m (or more) with both top and bottom surfaces trackable by the DDA-bifurcate [35]; therefore, there is no sensor-related or algorithm-related practical maximal depth limit to melt-pond detection on sea ice with ICESat-2 and the DDA-bif-seaice. The minimal pond depth is 0.5 m, a constraint that is associated with the 1.5-ns pulsewidth of the ATLAS sensor (1.5 ns equals 0.45 m at the speed of light) and implemented in the algorithm. Its computational efficiency suggests that a future version of the DDA-bif-seaice may be applied as an operational algorithm for the analysis of ICESat-2 ATLAS data across large regions, including the entire Arctic and Antarctic sea-ice regions. The problem of signal saturation is explained and needs to be addressed in future algorithm development, as currently saturation effects are partly avoided, but can also lead to false positives, especially in near-nadir central beams.

Melt ponds are not reported on the standard ICESat-2 ATLAS sea-ice products ATL07 (sea-ice surface heights) and ATL10 (sea-ice freeboard), because of the low along-track resolution of the products and because the ATL07 algorithm is designed to determine a single-surface height. The signal-noise separation algorithm of the DDA-bif-seaice identifies every photon as signal or noise (background) and hence retains the 0.7-m nominal photon spacing of the ICESat-2 point cloud, whereas the ATL07/10 algorithm relies on segments of 150 photons, typically between 17 m × 27 m and 17 m ×

200 m [22]. Thus, the DDA-bif-seaice can derive features with a much higher resolution than the ATL07/10 algorithm. To illustrate the increase in information, results from the DDA-bif-seaice are compared with results from the ATL07 algorithm. Because ATL10 results are derived from ATL07, ponded areas can be mistaken for open water, and thus, freeboard is miscalculated. Results from an advanced version of the DDA-bif-seaice analysis may be included in a future version of the standard ICESat-2 ATLAS data products. This may not only add information on the existence, location, depth, and size of ponds to the ICESat-2 sea-ice products but also facilitate the improvement of freeboard determination.

To demonstrate the capabilities of the DDA-bif-seaice as a fully automated algorithm for melt-pond detection that automatically adapts to changing background conditions, especially to the more challenging conditions of daylight, the DDA-bifurcate-seaice is applied to large ICESat-2 datasets from the 2019 and 2020 melt seasons in the multi-year Arctic sea-ice region (MYASIR). The analysis is carried out for about 10% of all ICESat-2 data collected in the summer of 2020 (outer strong beam data), which is considered representative of the entire ICESat-2 ATLAS dataset for this time frame and area. The results from the 2020 analysis yield approximately 10 200 ponds and are utilized in a large-scale study on the evolution of melt ponding [5].

As a means of evaluation, results from the DDA-bifseaice are compared with and integrated with results from UMD MPA, which is a computational algorithm for pond determination and depth measurement that requires a priori, manually determined information on locations where melt ponds exist. Agreement in pond location between the two algorithms is generally good. The DDA-bif-seaice finds a large multitude of the number ponds compared with the UMD MPA with sizes across all size ranges, while the MPA aids in finding larger, deeper ponds. A systematic difference of about 0.44 m in pond depths, with DDA depths generally larger, attributed to different physical-mathematical principles in lidar data analysis in the two algorithms, indicates that a field validation campaign is needed to resolve such depth uncertainties. The agreement is sufficient for the geophysical interpretation of trends in the pond evolution. The comparison further documents that the DDA-bif-seaice meets the criteria expected from a fully automated algorithm.

REFERENCES

- E. Buckley, "High resolution remote sensing observations of summer sea ice," Ph.D. thesis, Dept. Geograph. Sci. Atmos. Ocean. Sci., Univ. Maryland, College Park, MD, USA, 2022.
- [2] E. M. Buckley, S. L. Farrell, K. Duncan, L. N. Connor, J. M. Kuhn, and R. T. Dominguez, "Classification of sea ice summer melt features in high-resolution IceBridge imagery," *J. Geophys. Res., Oceans*, vol. 125, no. 5, May 2020, Art. no. e2019JC015738, doi: 10.1029/2019JC015738.
- [3] E. Buckley, S. Farrell, K. Duncan, and U. Herzfeld, "ICESat-2 observations of melt ponds on Arctic sea ice," in *Proc. Amer. Geophys. Union Fall Meeting*, Dec. 2020, pp. 7–11.
- [4] E. Buckley, S. Farrell, K. Duncan, U. Herzfeld, and M. Webster, "Sea ice melt pond properties as observed by ICESat-2," in *Proc. Amer. Geophys. Union Fall Meeting*, San Francisco, CA, USA, Dec. 2019, pp. 9–13.
- [5] E. M. Buckley et al., "Observing the evolution of summer melt on multiyear sea ice with ICESat-2 and Sentinel-2." Cryosphere, Feb. 2023.

- [6] S. L. Farrell, K. Duncan, E. M. Buckley, J. Richter-Menge, and R. Li, "Mapping sea ice surface topography in high fidelity with ICESat-2," *Geophys. Res. Lett.*, vol. 47, no. 21, Nov. 2020, Art. no. e2020GL090708, doi: 10.1029/2020GL090708.
- [7] F. Fetterer and N. Untersteiner, "Observations of melt ponds on Arctic sea ice," J. Geophys. Res., Oceans, vol. 103, no. C11, pp. 24821–24835, Oct. 1998, doi: 10.1029/98JC02034.
- [8] H. A. Fricker et al., "ICESat-2 meltwater depth estimates: Application to surface melt on Amery Ice Shelf, East Antarctica," *Geophys. Res. Lett.*, vol. 48, no. 8, Apr. 2021, Art. no. e2020GL090550, doi: 10.1029/2020GL090550.
- [9] U. Herzfeld, A. Hayes, S. Palm, D. Hancock, M. Vaughan, and K. Barbieri, "Detection and height measurement of tenuous clouds and blowing snow in ICESat-2 ATLAS data," *Geophys. Res. Lett.*, vol. 48, no. 17, 2021, Art. no. e2021GL093473, doi: 10.1029/2021GL093473.
- [10] U. C. Herzfeld et al., "Algorithm for detection of ground and canopy cover in micropulse photon-counting LiDAR altimeter data in preparation for the ICESat-2 mission," *IEEE Trans. Geosci. Remote Sens.*, vol. 52, no. 4, pp. 2109–2125, Apr. 2014, doi: 10.1109/TGRS.2013.2258350.
- [11] U. Herzfeld, S. Palm, D. Hancock, A. Hayes, and K. Barbieri, ICESat-2 Algorithm Theoretical Basis Document for the Atmosphere, Part II: Detection of Atmospheric Layers and Surface Using a Density Dimension Algorithm, document v13.0, version 118.0, 2021, doi: 10.5067/48PJ5OUJOP4C.
- [12] U. C. Herzfeld, T. M. Trantow, D. Harding, and P. W. Dabney, "Surface-height determination of crevassed glaciers—Mathematical principles of an autoadaptive density-dimension algorithm and validation using ICESat-2 simulator (SIMPL) data," *IEEE Trans. Geosci. Remote Sens.*, vol. 55, no. 4, pp. 1874–1896, Apr. 2017, doi: 10.1109/TGRS.2016.2617323.
- [13] U. Herzfeld, T. Trantow, M. Lawson, J. Hans, and G. Medley, "Surface heights and crevasse types of surging and fast-moving glaciers from ICESat-2 laser altimeter data—Application of the density-dimension algorithm (DDA-ice) and validation using airborne altimeter and Planet SkySat data," Sci. Remote Sens., vol. 3, pp. 1–20, Jun. 2021, doi: 10.1016/j.srs.2020.100013.
- [14] U. C. Herzfeld, M. Lawson, T. Trantow, and T. Nylen, "Airborne validation of ICESat-2 ATLAS data over crevassed surfaces and other complex glacial environments: Results from experiments of laser altimeter and kinematic GPS data collection from a helicopter over a surging Arctic glacier (Negribreen, Svalbard)," *Remote Sens.*, vol. 14, pp. 1185–1224, Feb. 2022, doi: 10.3390/rs14051185.
- [15] U. C. Herzfeld, J. A. Maslanik, and M. Sturm, "Geostatistical characterization of snow-depth structures on sea ice near point barrow, Alaska—A contribution to the AMSR-Ice03 field validation campaign," *IEEE Trans. Geosci. Remote Sens.*, vol. 44, no. 11, pp. 3038–3056, Nov. 2006, doi: 10.1109/TGRS.2006.883349.
- [16] M. M. Holland, D. A. Bailey, B. P. Briegleb, B. Light, and E. Hunke, "Improved sea ice shortwave radiation physics in CCSM4: The impact of melt ponds and aerosols on Arctic sea ice," *J. Climate*, vol. 25, no. 5, pp. 1413–1430, Mar. 2012, doi: 10.1175/JCLI-D-11-00078.1.
- [17] E. C. Hunke, W. H. Lipscomb, A. K. Turner, N. Jeffery, and S. Elliott, "CICE: The Los Alamos sea ice model, documentation and software, version 5.0," Los Alamos Nat. Lab., Los Alamos, NM, USA, Tech. Rep., LA-CC-06-012, 2013, [Online]. Available: http://oceans11.lanl.gov/trac/CICE/attachment/wiki/WikiStart/cicedoc. pdf?format=raw
- [18] A. Jahn et al., "Late-twentieth-century simulation of Arctic sea ice and ocean properties in the CCSM4," *J. Climate*, vol. 25, no. 5, pp. 1431–1452, Mar. 2012.
- [19] J. E. Kay, M. M. Holland, and A. Jahn, "Inter-annual to multi-decadal Arctic sea ice extent trends in a warming world," *Geophys. Res. Lett.*, vol. 38, no. 15, Aug. 2011.
- [20] R. Kwok, "Arctic sea ice thickness, volume, and multiyear ice coverage: Losses and coupled variability (1958–2018)," *Environ. Res. Lett.*, vol. 13, no. 10, 2018, Art. no. 105005.
- [21] R. Kwok et al., "ICESat-2 surface height and sea ice freeboard assessed with ATM LiDAR acquisitions from operation IceBridge," *Geophys. Res. Lett.*, vol. 46, no. 20, pp. 11228–11236, Oct. 2019.
- [22] R. Kwok et al., "Surface height and sea ice freeboard of the Arctic Ocean from ICESat-2: Characteristics and early results," J. Geophys. Res., Oceans, vol. 124, no. 10, pp. 6942–6959, 2019.
- [23] R. Kwok et al., "ICESat-2 algorithm theoretical basis document for sea ice products," ICESat-2 Project, NASA, Washington, DC, USA, Nov. 2021, doi: 10.5067/189WL8W8WRH8.

- [24] R. Kwok et al., "ATLAS/ICESat-2 L3A sea ice freeboard, version 5," 2020, doi: 10.5067/ATLAS/ATL10.005.
- [25] R. Kwok et al., "ATLAS/ICESat-2 L3A sea ice height, version 5," 2019, doi: 10.5067/ATLAS/ATL07.005.
- [26] L. Magruder, K. N. T. Brunt, B. Klotz, and M. Alonzo, "ICESat-2 early mission synopsis and observatory performance," *Earth Space Sci.*, vol. 8, pp. 1–10, Jan. 2021, doi: 10.1029/2020EA001414.
- [27] T. Markus et al., "The ice, cloud, and land elevation satellite-2 (ICESat-2): Science requirements, concept, and implementation," *Remote Sens. Environ.*, vol. 190, pp. 260–273, Mar. 2017, doi: 10.1016/j.rse.2016.12.029.
- [28] T. Markus, J. C. Stroeve, and J. Miller, "Recent changes in Arctic sea ice melt onset, freezeup, and melt season length," *J. Geophys. Res.*, vol. 114, no. C12, pp. 1–14, 2009, doi: 10.1029/2009JC005436.
- [29] J. A. Maslanik et al., "Spatial variability of barrow-area shore-fast sea ice and its relationships to passive microwave emissivity," *IEEE Trans. Geosci. Remote Sens.*, vol. 44, no. 11, pp. 3021–3031, Nov. 2006, doi: 10.1109/TGRS.2006.879557.
- [30] T. Neumann et al., "ATLAS/ICESat-2 L2A global geolocated photon data, version 5," Tech. Rep., 2021.
- [31] T. Neumann et al., "ICESat-2 algorithm theoretical basis document for global geolocated photons ATL03, release 005," ICESat-2 Project, NASA, Washington, DC, USA, Tech. Rep., 2021, doi: 10.5067/D0VQW9KX3GTU.
- [32] T. A. Neumann et al., "The ice, cloud, and land elevation satellite-2 mission: A global geolocated photon product derived from the advanced topographic laser altimeter system," *Remote Sens. Environ.*, vol. 233, Nov. 2019, Art. no. 111325, doi: 10.1016/j.rse.2019. 111325.
- [33] D. Notz and S. Community, "Arctic sea ice in CMIP6," *Geophys. Res. Lett.*, vol. 47, no. 10, May 2020, Art. no. e2019GL086749.
- [34] S. P. Palm et al., "ICESat-2 atmospheric channel description, data processing and first results," *Earth Space Sci.*, vol. 8, no. 8, pp. 1–10, Aug. 2021, doi: 10.1029/2020EA001470.
- [35] C. Parrish et al., "ICESat-2 bathymetry: Advances in methods and science," in *Proc. OCEANS*, Oct. 2022, pp. 1–6.
- [36] D. K. Perovich, "Thin and thinner: Sea ice mass balance measurements during SHEBA," J. Geophys. Res., vol. 108, no. C3, pp. 1–21, 2003, doi: 10.1029/2001JC001079.
- [37] D. K. Perovich, "Seasonal evolution of the albedo of multiyear Arctic sea ice," J. Geophys. Res., vol. 107, no. C10, pp. 1–13, 2002, doi: 10.1029/2000JC000438.
- [38] D. K. Perovich and C. Polashenski, "Albedo evolution of seasonal Arctic sea ice," *Geophys. Res. Lett.*, vol. 39, no. 8, pp. 1–14, Apr. 2012, doi: 10.1029/2012GL051432.
- [39] D. K. Perovich, "Aerial observations of the evolution of ice surface conditions during summer," *J. Geophys. Res.*, vol. 107, no. C10, pp. 1–22, 2002, doi: 10.1029/2000JC000449.
- [40] A. A. Petty et al., "The Arctic sea ice cover of 2016: A year of record-low highs and higher-than-expected lows," *Cryosphere*, vol. 12, no. 2, pp. 433–452, Feb. 2018.
- [41] C. Polashenski, D. Perovich, and Z. Courville, "The mechanisms of sea ice melt pond formation and evolution," *J. Geophys. Res.*, *Oceans*, vol. 117, no. C1, pp. 1–21, Jan. 2012, doi: 10.1029/ 2011JC007231.
- [42] A. Rösel and L. Kaleschke, "Exceptional melt pond occurrence in the years 2007 and 2011 on the Arctic sea ice revealed from MODIS satellite data," *J. Geophys. Res., Oceans*, vol. 117, no. C5, pp. 1–8, May 2012, doi: 10.1029/2011JC007869.
- [43] A. Rösel, L. Kaleschke, and G. Birnbaum, "Melt ponds on Arctic sea ice determined from MODIS satellite data using an artificial neural network," *Cryosphere*, vol. 6, no. 2, pp. 431–446, Apr. 2012, doi: 10.5194/tc-6-431-2012.
- [44] F. Scott and D. L. Feltham, "A model of the three-dimensional evolution of Arctic melt ponds on first-year and multiyear sea ice," *J. Geophys. Res., Oceans*, vol. 115, no. C12, pp. 1–12, Dec. 2010, doi: 10.1029/2010JC006156.
- [45] M. C. Serreze, M. M. Holland, and J. Stroeve, "Perspectives on the Arctic's shrinking sea-ice cover," *Science*, vol. 315, no. 5818, pp. 1533–1536, Mar. 2007.
- [46] M. Serreze, W. Meier, J. Stroeve, T. Scambos, and S. Renfrow, "Arctic Sea ice in 2008: Standing on the threshold," in *Proc. AGU Fall Meeting Abstr.*, vol. 1, 2008, p. 1.
- [47] B. E. Smith, A. Gardner, A. Schneider, and M. Flanner, "Modeling biases in laser-altimetry measurements caused by scattering of green light in snow," *Remote Sens. Environ.*, vol. 215, pp. 398–410, Sep. 2018.

- [48] J. Stroeve, M. M. Holland, W. Meier, T. Scambos, and M. Serreze, "Arctic sea ice decline: Faster than forecast," *Geophys. Res. Lett.*, vol. 34, no. 9, p. 9501, May 2007, doi: 10.1029/2007GL029703.
- [49] J. Stroeve and D. Notz, "Changing state of Arctic sea ice across all seasons," *Environ. Res. Lett.*, vol. 13, no. 10, Sep. 2018, Art. no. 103001.
- [50] J. C. Stroeve, M. C. Serreze, M. M. Holland, J. E. Kay, J. Malanik, and A. P. Barrett, "The Arctic's rapidly shrinking sea ice cover: A research synthesis," *Climatic Change*, vol. 110, nos. 3–4, pp. 1005–1027, Feb. 2012.
- [51] M. Sturm et al., "Snow depth and ice thickness measurements from the Beaufort and Chukchi Seas collected during the AMSR-Ice03 campaign," *IEEE Trans. Geosci. Remote Sens.*, vol. 44, no. 11, pp. 3009–3020, Nov. 2006.
- [52] R. Tilling, N. T. Kurtz, M. Bagnardi, A. A. Petty, and R. Kwok, "Detection of melt ponds on Arctic summer sea ice from ICESat-2," *Geophys. Res. Lett.*, vol. 47, no. 23, Dec. 2020, Art. no. e2020GL090644.
- [53] M. A. Tschudi, J. A. Maslanik, and D. K. Perovich, "Derivation of melt pond coverage on Arctic sea ice using MODIS observations," *Remote Sens. Environ.*, vol. 112, no. 5, pp. 2605–2614, May 2008, doi: 10.1016/j.rse.2007.12.009.
- [54] M. A. Webster et al., "Spatiotemporal evolution of melt ponds on Arctic sea ice: MOSAiC observations and model results," *Elementa*, Sci. Anthropocene, vol. 10, no. 1, May 2022, Art. no. 000072, doi: 10.1525/elementa.2021.000072.
- [55] M. A. Webster, I. G. Rigor, D. K. Perovich, J. A. Richter-Menge, C. M. Polashenski, and B. Light, "Seasonal evolution of melt ponds on Arctic sea ice," *J. Geophys. Res., Oceans*, vol. 120, no. 9, pp. 5968–5982, Sep. 2015, doi: 10.1002/2015JC011030.



Ute Christina Herzfeld received the master's degree in Mathematics, Evangelical Theology and Education and the Dr. rer. nat. degree in Mathematics with Applied Mathematics and Geosciences from the Johannes Gutenberg Universität Mainz, Germany, in 1983 and 1986, respectively. She is Director of the Geomathematics, Remote Sensing and Cryospheric Sciences Laboratory and a Research Professor at the Department of Electrical, Computer, and Energy Engineering, University of Colorado Boulder, Boulder, CO, USA. She is a geomathematician and

glaciologist with extensive field experience in high-latitude glaciers and ice streams, including expeditions to Antarctica, Greenland, Svalbard and Alaska. Her research interests include the development of algorithms for remotesensing data analysis, innovative aerial and satellite observation techniques and studies of fast-moving and surging glaciers and Arctic sea ice. She is a principal investigator on both the NASA ICESat-2 and the NASA Cloud-Sat/CALIPSO science teams. She is a member of the IEEE's Geoscience and Remote Sensing Society, the American Geophysical Union, the International Glaciological Society and the International Association for Mathematical Geosciences.



Thomas M. Trantow was born in Gunnison, CO, USA, in March 1990. He received the concurrent M.S. and B.S. degree in Applied Mathematics and the Ph.D. degree in Geophysics from the University of Colorado, Boulder, CO, USA, in 2014 and 2020, respectively, under the advisory of Prof. Ute Herzfeld. His research interests include remote sensing of glaciers and ice sheets, algorithm development and numerical modeling of ice dynamics. He participated in field work over Bering Glacier, Alaska, and Negribreen, Svalbard. He is a

member of the American Geophysical Union.



Huilin Han is a Graduate Research Assistant at the Geomathematics, Remote Sensing and Cryospheric Sciences Laboratory, University of Colorado Boulder, Boulder, CO, USA. She is currently pursuing the master's Degree in Computer Science from the University of Colorado Boulder.



Sinéad Louise Farrell received the M.Sc. degree in earth and space science and the Ph.D. degree from University College London, U.K., in 2002 and 2007, respectively. She is an Associate Professor in the Departments of Geographical Sciences and Atmospheric and Oceanic Science, University of Maryland, College Park, MD. She is a principal investigator on both the NASA ICESat-2 and the NASA/NOAA Ocean Surface Topography Science Teams. She serves as a member of the Mission Advisory Group for the European Copernicus Polar

Ice and Snow Topography Altimeter (CRISTAL) mission. Her research interests lie in remote sensing of the Earth's polar regions to study cryospheric and oceanic processes. She is a member of the American Geophysical Union.



Ellen Buckley is a Postdoctoral Researcher at Brown University, Center for Fluid Mechanics. Her research involves extracting information from remote sensing observations towards an improved understanding of the changing Arctic sea ice cover.



Matthew Lawson received the Bachelor of Science in Computer Sciences with Honors from the University of Colorado Boulder, Boulder, CO, USA, in August 2020. From 2020 to July 2021, he was a Professional Research Assistant at the Geomathematics, Remote Sensing and Cryospheric Sciences Laboratory, University of Colorado Boulder. He participated in the 2019 Airborne Geophysical Field Campaign over Negribreen, Svalbard, for ICESat-2 data evaluation. His research concerns algorithm development for ICESat-2, parallelization, and cloud processing.